nature materials

Supplementary information

https://doi.org/10.1038/s41563-025-02213-x

Immune-compatible designs of semiconducting polymers for bioelectronics with suppressed foreign-body response

In the format provided by the authors and unedited

Table of Contents

Supplementary Methods

Monomer synthesis

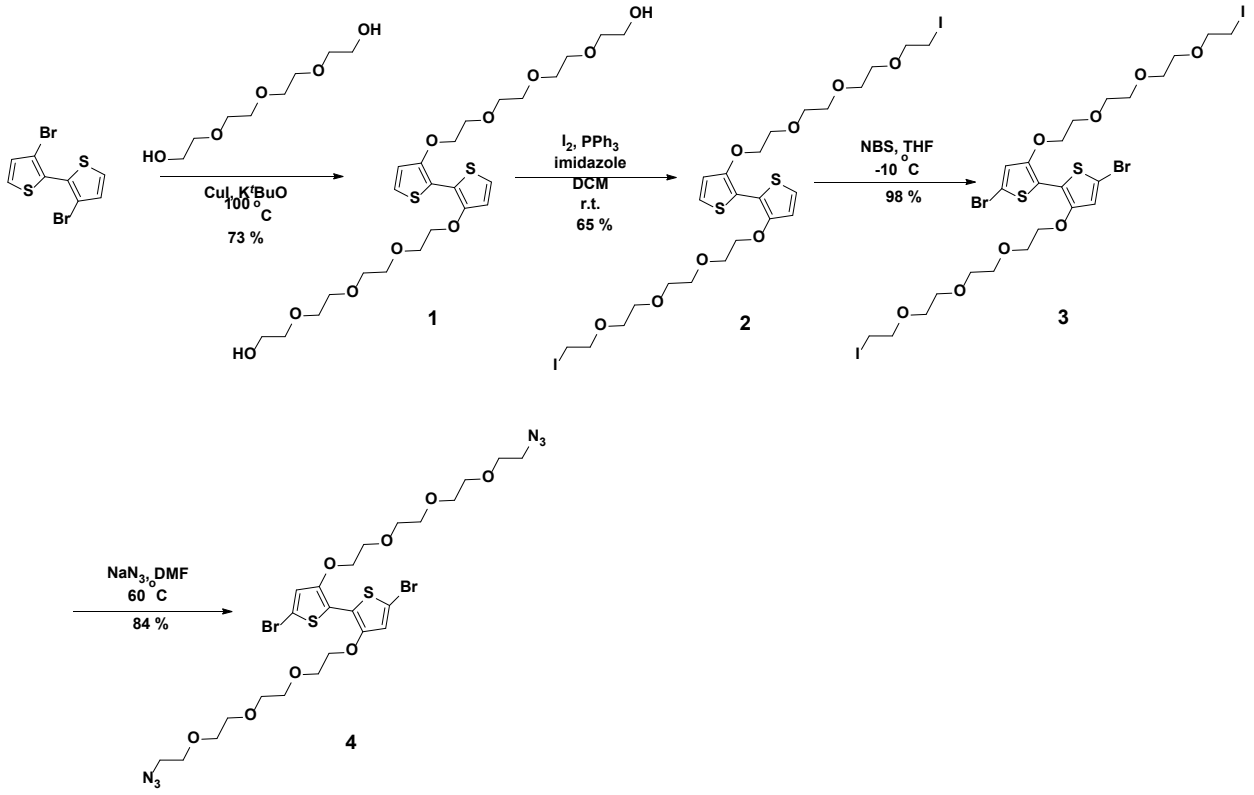

2,2'-(((((((([2,2'-bithiophene]-3,3'-diylbis(oxy))bis(ethane-2,1-diyl))bis(oxy))bis(ethane-2,1-diyl))bis(oxy))bis(ethane-2,1-diyl))bis(oxy))bis(ethan-1-ol) (1)

To a nitrogen gas filled round bottom flask (RBF) with a stirring bar, potassium *tert*-butoxide (37.3 mmol, 4.2 g), copper (I) iodide (5 mmol, 0.95 g), 3,3′-dibromo-2,2′-bithiophene (12.4 mmol, 4 g), and tetra(ethylene glycol) (12.4 mmol, 24 g) were added. The mixture was heated to 100 ºC for 20 h. Then the mixture was cooled to room temperature and filtered. The solid was washed with DCM and the organic phase was washed with 1M HCl and brine successively. The solvent was removed using rotary evaporation and purified by column chromatography (silica gel, EA). The final solid was isolated as a yellow oil (5 g, 73 %). ^{1}H NMR (400 MHz, $CDCl_3$) δ 7.07 (d, J = 5.5 Hz, 2H), 6.85 (d, J = 5.5 Hz, 2H), 4.25 (t, J = 4.8 Hz, 4H), 3.90 (t, J = 4.8 Hz, 4H), 3.79 – 3.72 (m, 4H), 3.72 – 3.62 (m, 16H), 3.62 – 3.55 (m, 4H), 2.46 (s, 2H); ^{13}C NMR (101 MHz, $CDCl_3$) δ 151.74, 121.94, 116.59, 115.00, 114.72, 72.47, 71.40, 70.93, 70.67, 70.38, 70.06, 61.76. HRMS (ESI) Calcd for $C_{24}H_{39}O_{10}S_2$ [M+H]+ : 551.1979, found 551.1989.

1D ^{1}H NMR spectrum for 1

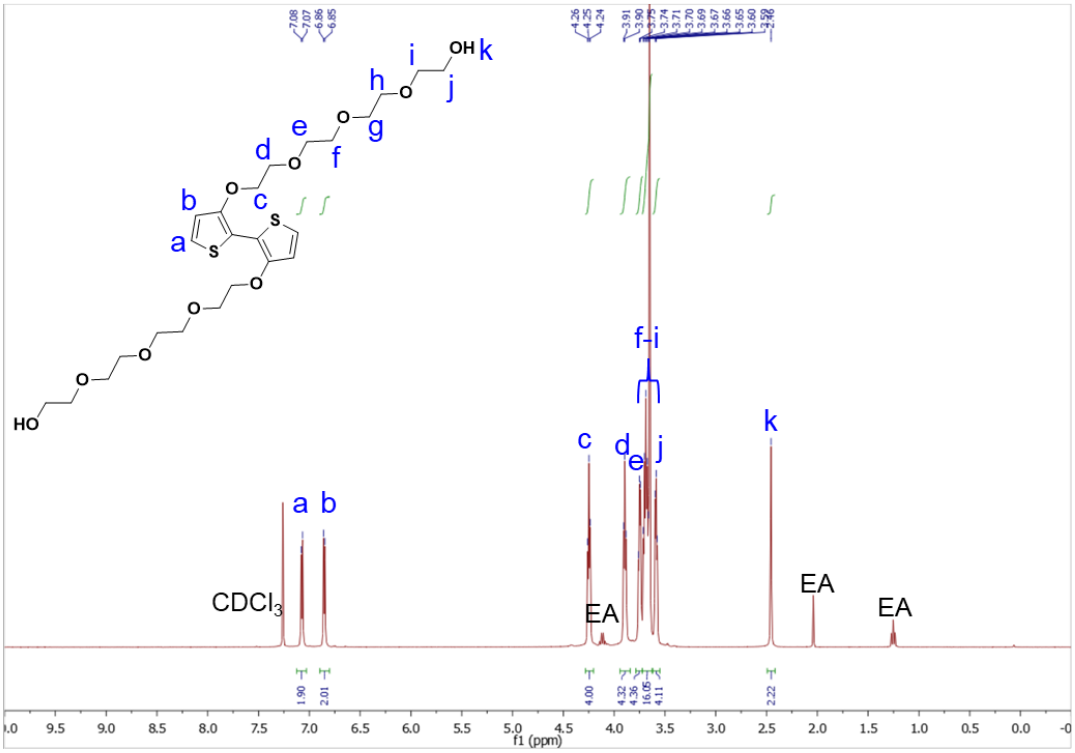

1D ^{13}C NMR spectrum for 1

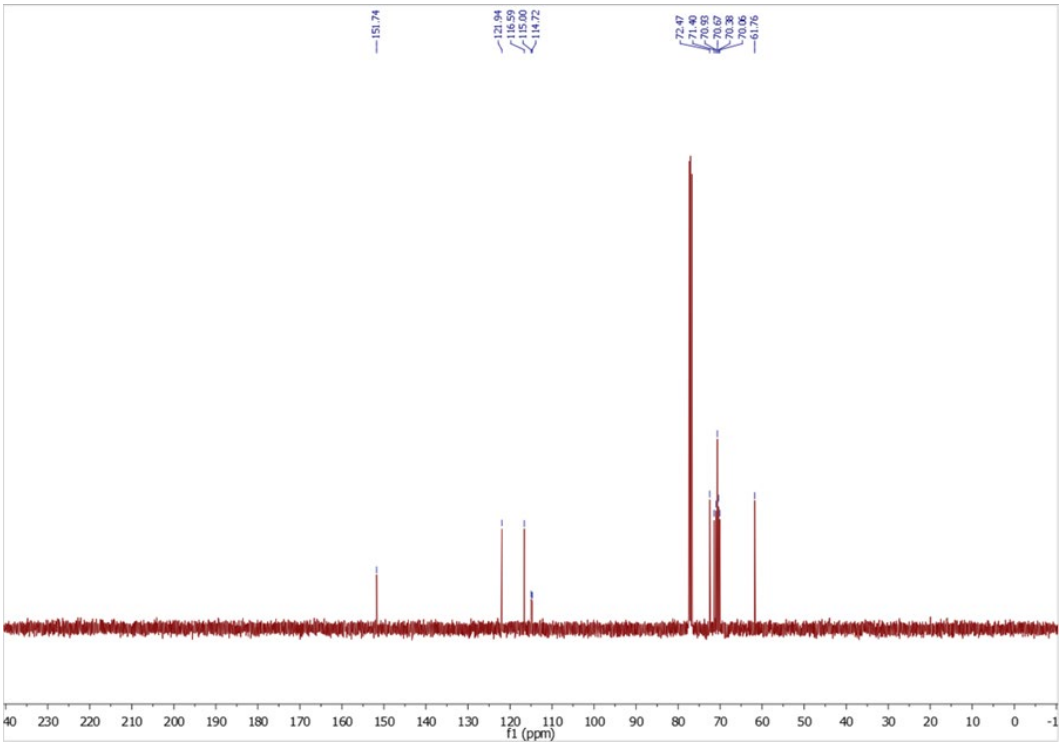

3,3'-bis(2-(2-(2-(2-iodoethoxy)ethoxy)ethoxy)ethoxy)-2,2'-bithiophene (2)

To a nitrogen gas filled RBF with I_2 (14.2 mmol, 3.6 g), imidazole (16.4 mmol, 1.1 g), and **1** (5.4 mmol, 3 g) in 40 mL DCM, PPh_3 (13.1 mmol, 3.4 g) in DCM was added at 0 ºC. The mixture was stirred at room temperature overnight. After that, the organic phase was washed with brine. The solvent was removed using rotary evaporation and purified by column chromatography (silica gel, EA/hexane = 1/1). The final solid was isolated as a yellow oil (2.4 g, 65 %). ^{1}H NMR (400 MHz, $CDCl_3$) δ 7.08 (d, *J* = 5.6 Hz, 2H), 6.85 (d, *J* = 5.6 Hz, 2H), 4.29 – 4.19 (m, 4H), 3.96 – 3.86 (m, 4H), 3.74 (dt, J = 9.5, 5.8 Hz, 8H), 3.71 – 3.60 (m, 12H), 3.30 – 3.18 (m, 4H). ^{13}C NMR (101 MHz, $CDCl_3$) δ 150.21, 119.65, 115.85, 110.06, 71.71, 70.95, 70.79, 70.73, 70.04, 69.89, 50.70. HRMS (ESI) Calcd for $C_{24}H_{37}I_2O_8S_2$ [M+H]+ : 771.0014, found 771.0022.

1D ^{1}H NMR spectrum for 2

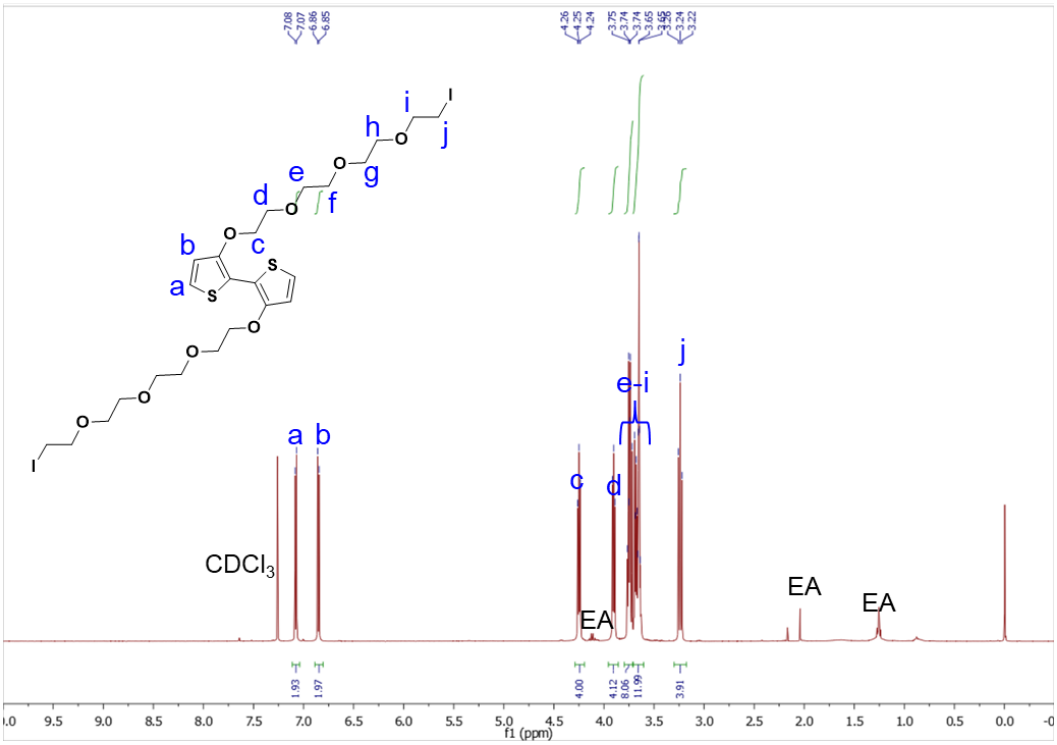

1D ^{13}C NMR spectrum for 2

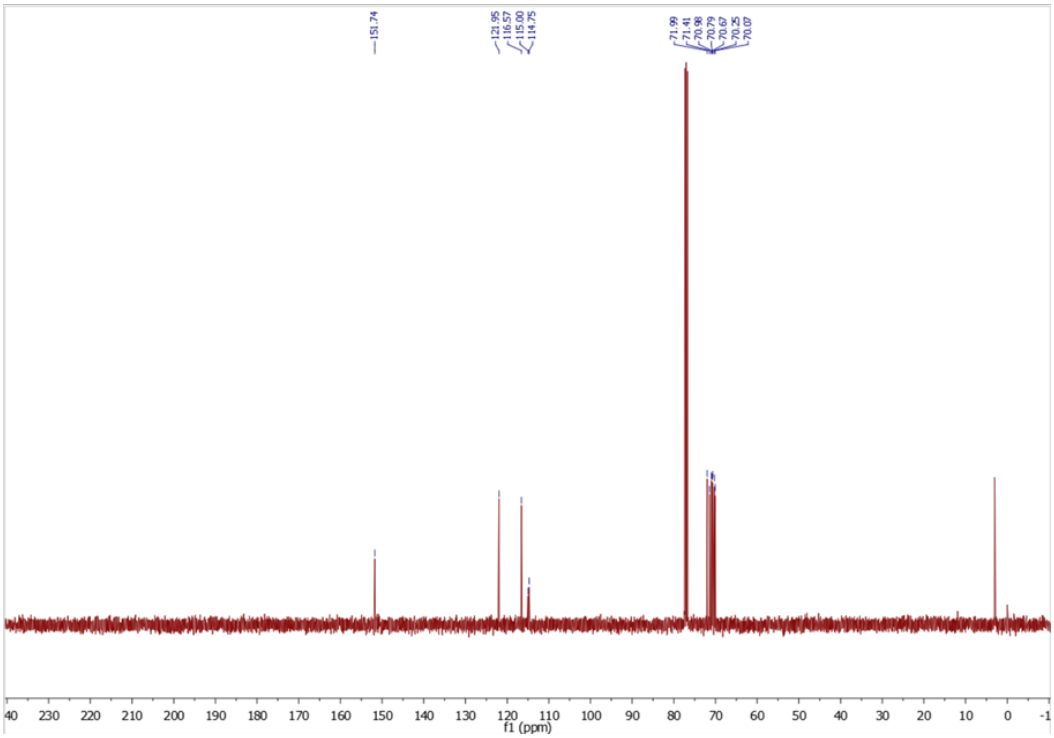

5,5'-dibromo-3,3'-bis(2-(2-(2-(2-iodoethoxy)ethoxy)ethoxy)ethoxy)-2,2'-bithiophene (3)

To a nitrogen gas filled RBF, **2** (2.2 mmol, 1.5 g) was dissolved in 30 mL THF and cooled to -10 ºC. NBS (4.6 mmol, 0.81 g) in 10 mL THF was added to the solution dropwise. The mixture was stirred at room temperature for 2 h. Then the mixture was quenched with sodium sulfite aqueous solution. The mixture was washed with brine and extracted with DCM. The solvent was removed using rotary evaporation and purified by column chromatography (silica gel, EA/hexane = 1/1). The final solid was isolated as a yellow oil (1.8 g, 98 %). ^{1}H NMR (400 MHz, $CDCl_3$) δ 6.85 (s, 2H), 4.25 – 4.13 (m, 4H), 3.93 – 3.83 (m, 4H), 3.72 (ddd, *J* = 15.0, 13.3, 8.4 Hz, 20H), 3.25 (t, *J* = 6.9 Hz, 4H); ^{13}C NMR (101 MHz, $CDCl_3$) δ 150.20, 119.65, 115.85, 110.07, 72.00, 71.72, 70.97, 70.80, 70.72, 70.27, 69.92. HRMS (ESI) Calcd for $C_{24}H_{35}Br_2I_2O_8S_2$ [M+H]+ : 926.8224, found 926.8225.

1D ^{1}H NMR spectrum for 3

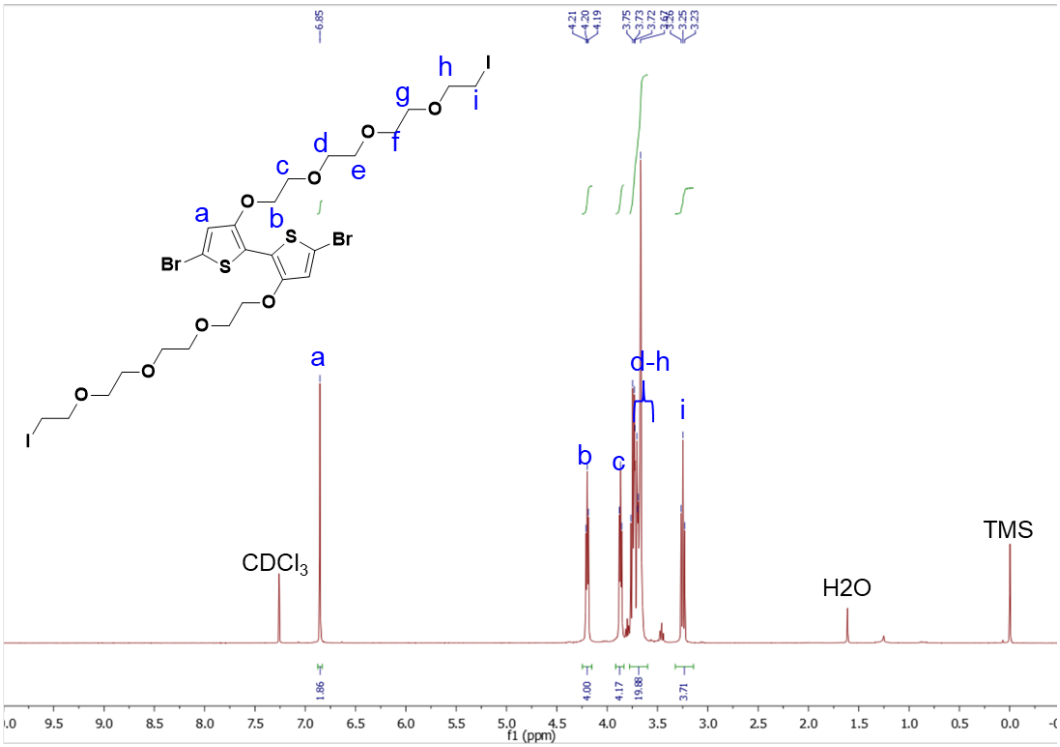

1D ^{13}C NMR spectrum for 3

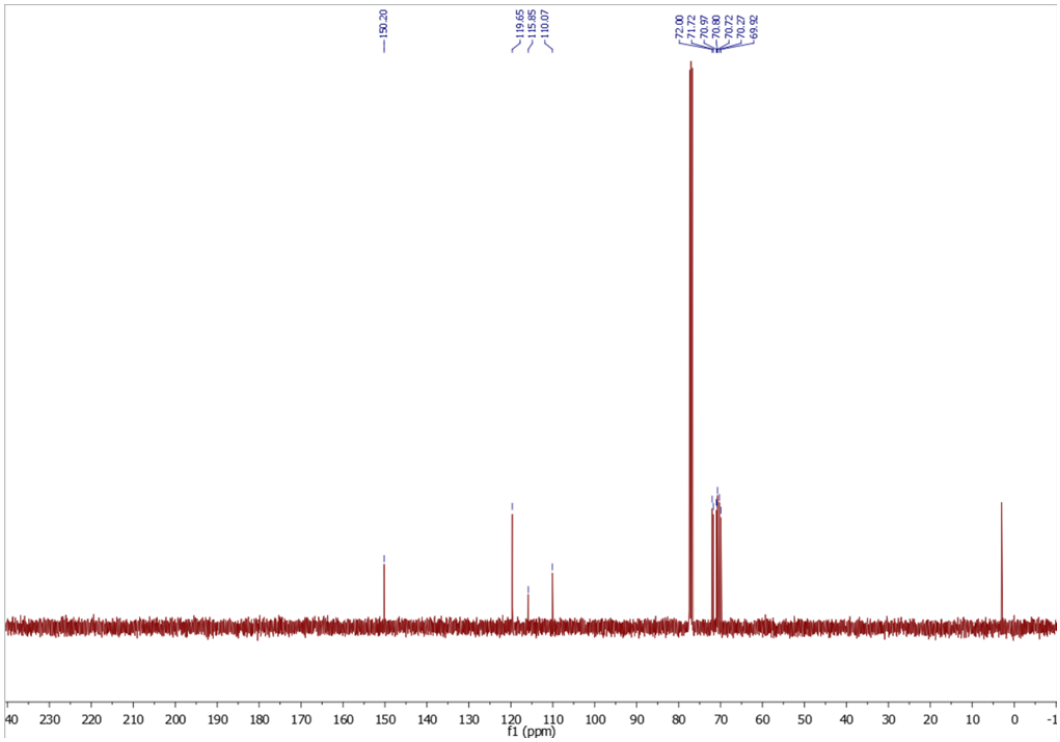

3,3'-bis(2-(2-(2-(2-azidoethoxy)ethoxy)ethoxy)ethoxy)-5,5'-dibromo-2,2'-bithiophene (4)

To a nitrogen gas filled RBF, **3** (1.2 mmol, 1 g) was dissolved in 30 mL DMF. NaN_3 (7.2 mmol, 0.47 g) in 10 mL DMF was added to the solution dropwise. The mixture was stirred at 60 ºC overnight. The mixture was washed with brine and extracted with DCM. The solvent was removed using rotary evaporation and purified by column chromatography (silica gel, EA/hexane = 1/1). The final solid was isolated as a yellow oil (0.76 g, 84 %). ^{1}H NMR (400 MHz, $CDCl_3$) δ 6.85 (s, 2H), 4.20 (t, J = 4.7 Hz, 4H), 3.87 (t, J = 4.7 Hz, 4H), 3.78 – 3.61 (m, 20H), 3.38 (t, J = 4.9 Hz, 4H); ^{13}C NMR (101 MHz, $CDCl_3$) δ 150.21, 119.65, 115.85, 110.06, 71.71, 70.95, 70.79, 70.73, 70.04, 69.89, 50.70. HRMS (ESI) Calcd for $C_{24}H_{35}Br_2N_6O_8S_2$ [M+H]+ : 757.0319, found 757.0302.

1D ^{1}H NMR spectrum for 4

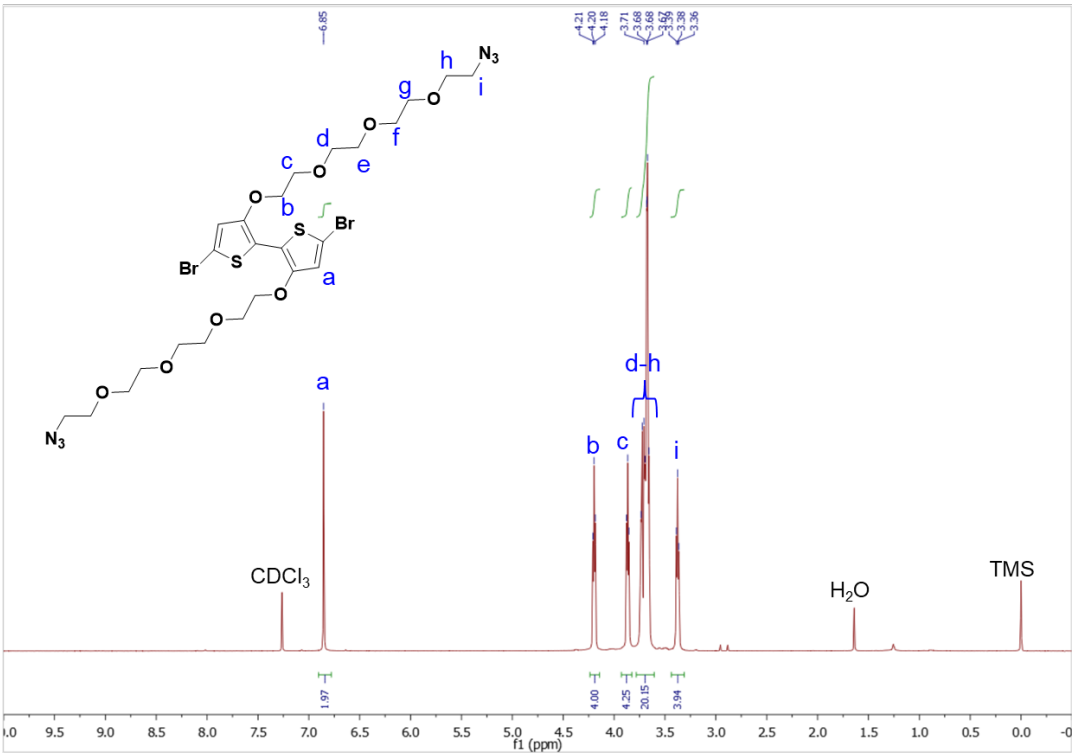

1D ^{13}C NMR spectrum for 4

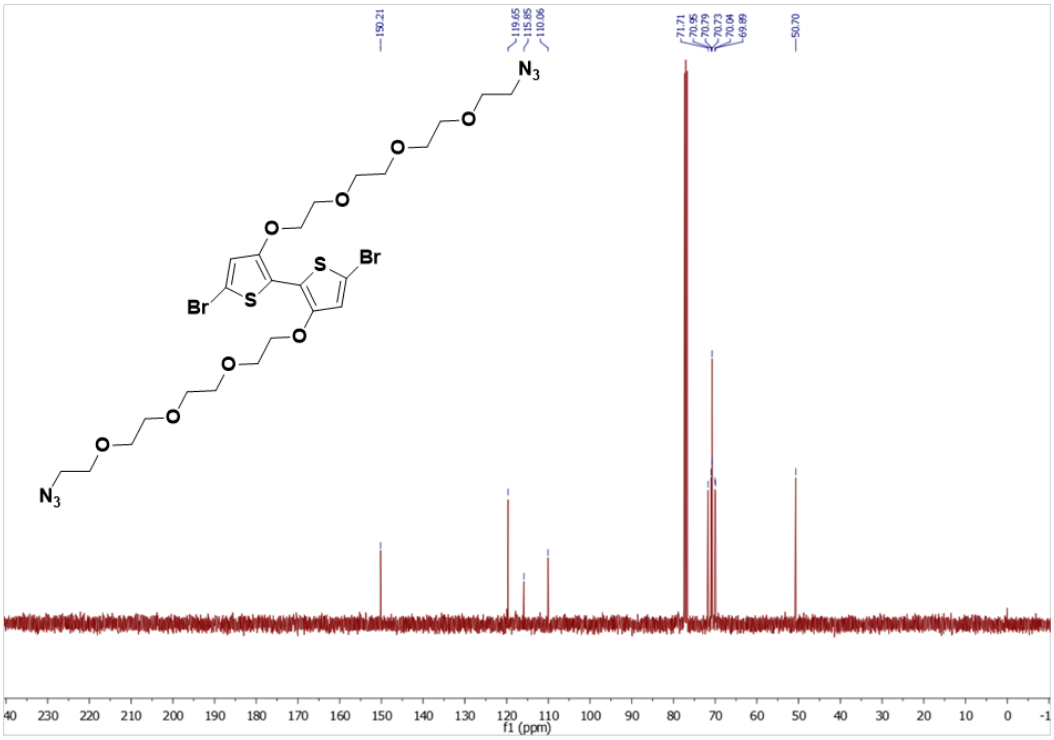

2D COSY NMR spectrum for 4

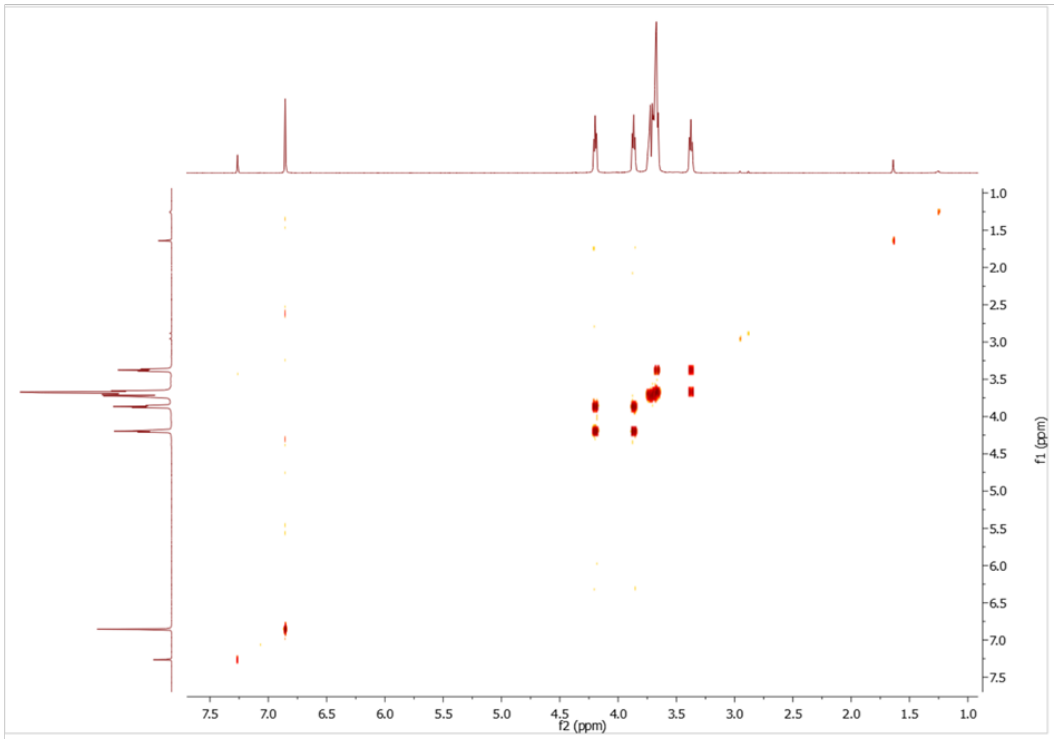

2,5-bis(trimethylstannyl)selenophene

To a nitrogen gas filled RBF with selenophene (10 mmol, 1.3 g) in THF, *n*-butyllithium (21.8 mmol, 12.8 mL) was added dropwise at -78 ºC. The reaction was stirred at r.t. for 30 min. The mixture was cooled to -78 ºC. Trimethyltin chloride (25 mmol, 25 mL) was then added dropwise. The mixture was warmed to r.t and stirred overnight. After that, the mixture was poured into water and was extracted with diethyl ether. The organic phase was then concentrated. The final product was recrystallized from methanol as white solids (1.5 g, 33 %). ^{1}H NMR (400 MHz, $CDCl_3$) δ 7.68 (s, 2H), 0.47 – 0.27 (m, 18H). ^{13}C NMR (101 MHz, $CDCl_3$) δ 150.18, 138.70, -7.78.

1D ^{1}H NMR spectrum for 2,5-bis(trimethylstannyl)selenophene

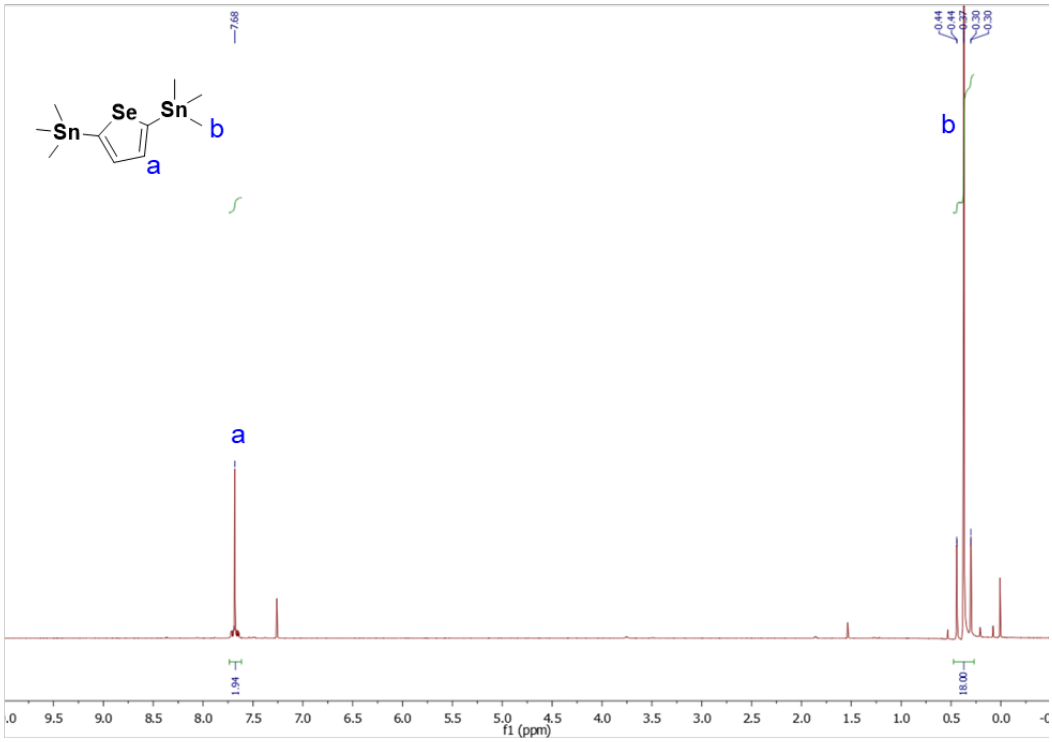

1D ^{13}C NMR spectrum for 2,5-bis(trimethylstannyl)selenophene

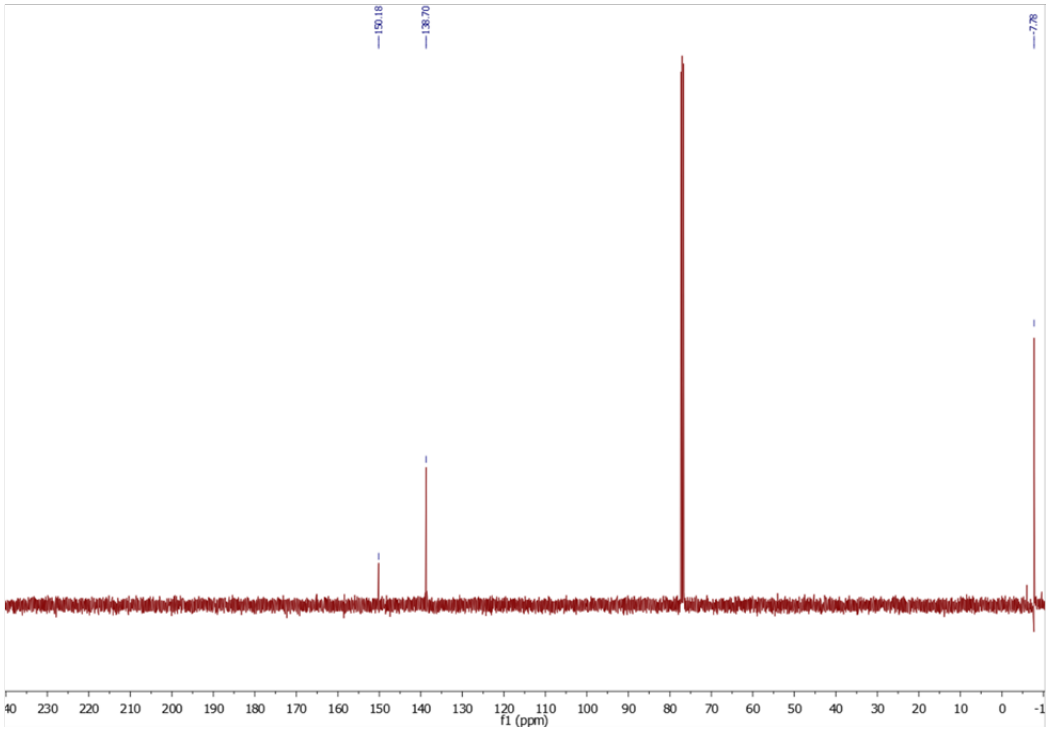

Polymer synthesis

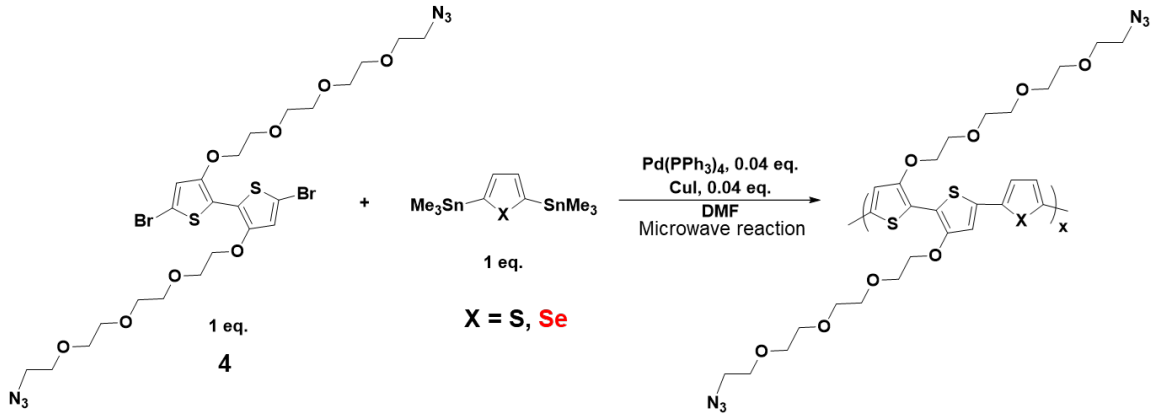

To a mixture of **4** (50 mg, 0.0774 mmol, 1.0 eq.), 2,5-bis(trimethylstannyl)thiophene (31.9 mg, 0.0774 mmol, 1.0 eq.), (or 2,5-bis(trimethylstannyl)selenophene (35.6 mg, 0.0774 mmol, 1.0 eq.)), $Pd(PPh_3)_4$ (3.6 mg, 0.0031 mmol, 0.04 eq.), and CuI (0.6 mg, 0.0031 mmol, 0.04 eq.) was added 2 mL of anhydrous DMF in a nitrogen filled glovebox. The reaction vial was sealed and submitted to a microwave reactor with the following temperature profile: 2 min at 80 °C and 6 min at 100 °C. After the reaction was cooled down, 10 mol% of trimethyl(phenyl)stannane were added and the crude polymer solution was heated again to 2 min at 80 °C. To complete the end-capping of the polymer, 10 mol% of bromobenzene were added and the reaction vessel submitted one last time to microwave heating (2 min at 80 °C). The crude polymer was then precipitated into methanol, filtered, loaded to a Soxhlet thimble and washed successively with hexane, ethyl acetate (each for 24 h). The polymer was finally collected from the thimble with chloroform. The chloroform solution was then concentrated to give the blue polymer named as p(g2T-T)-a or p(g2T-Se)-a. The molecular weights are listed in the Supplementary Table 2.

1D ^{1}H NMR spectrum for p(g2T-T)-a polymer

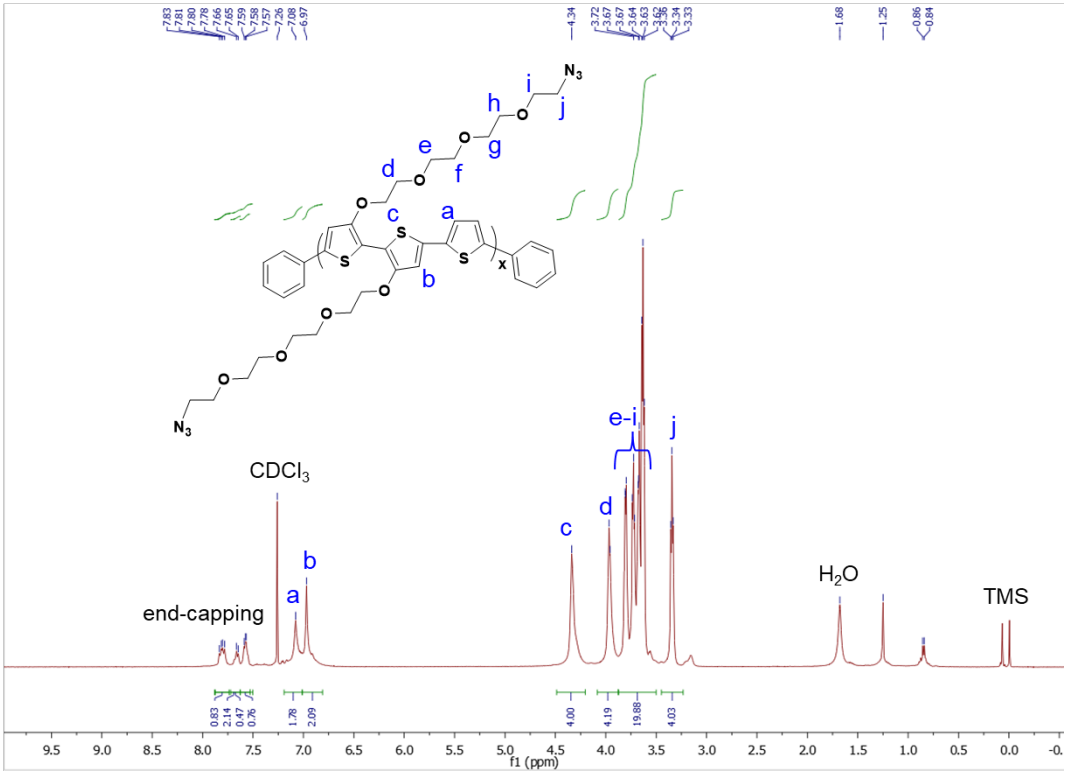

2D COSY NMR spectrum for p(g2T-T)-a polymer

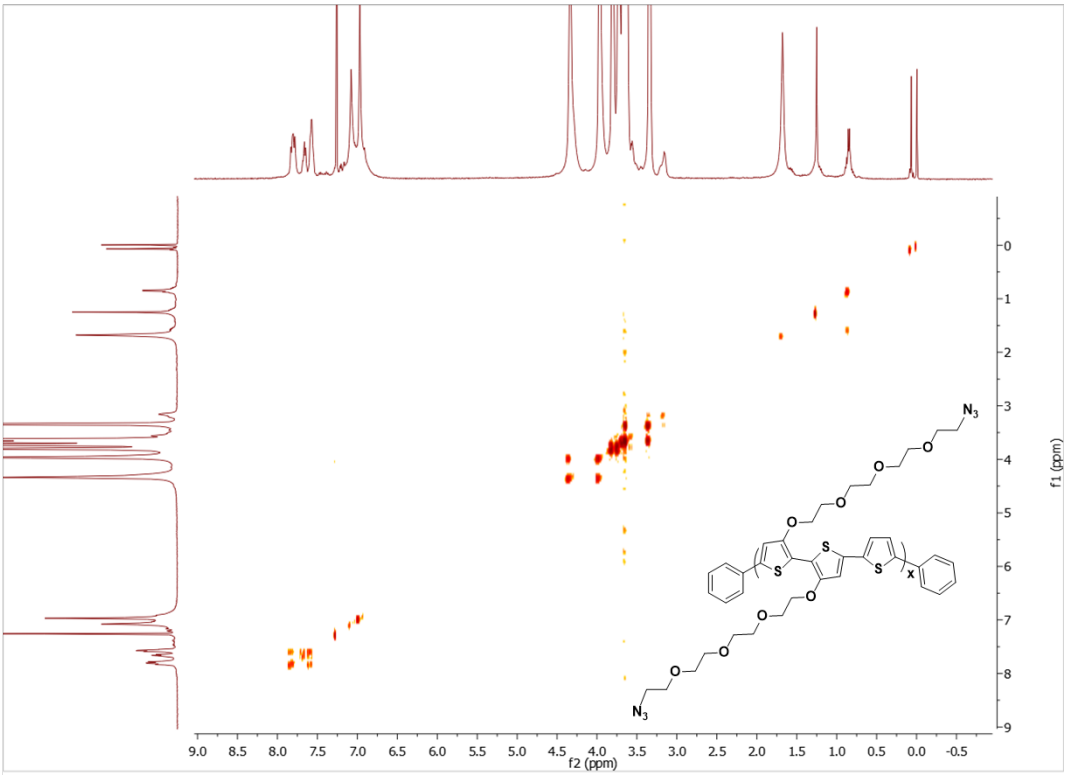

1D ^{1}H NMR spectrum for p(g2T-Se)-a polymer

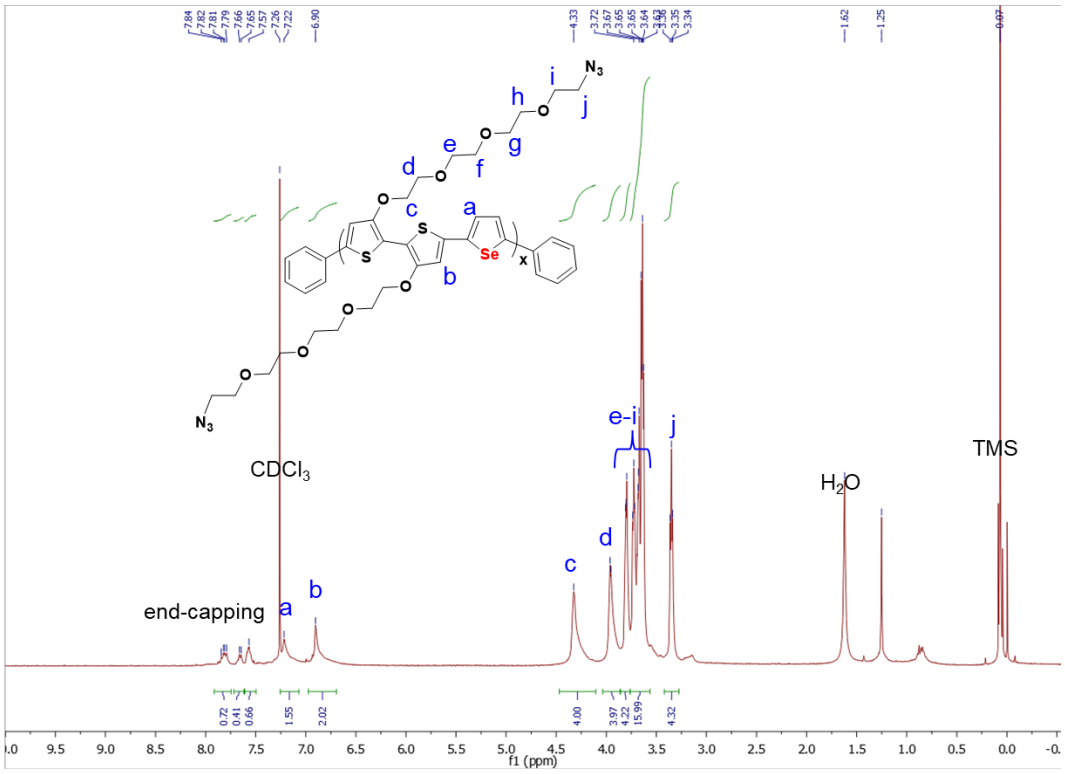

2D COSY NMR spectrum for p(g2T-Se)-a polymer

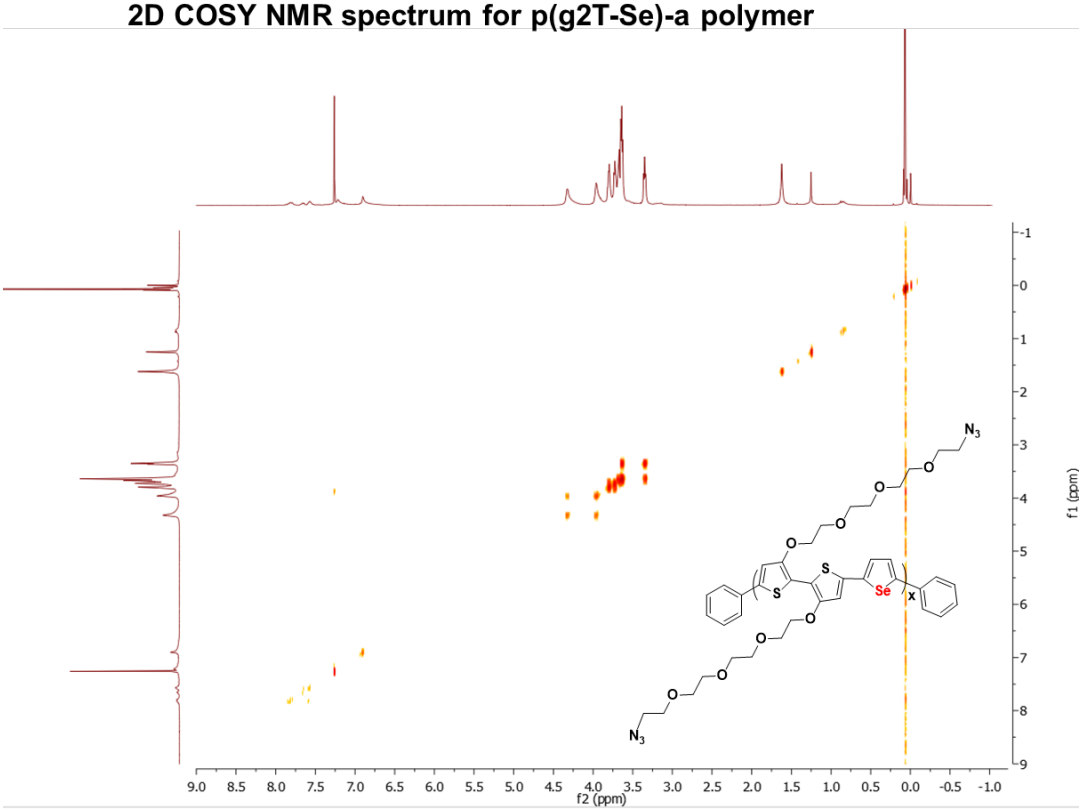

Supplementary Figures

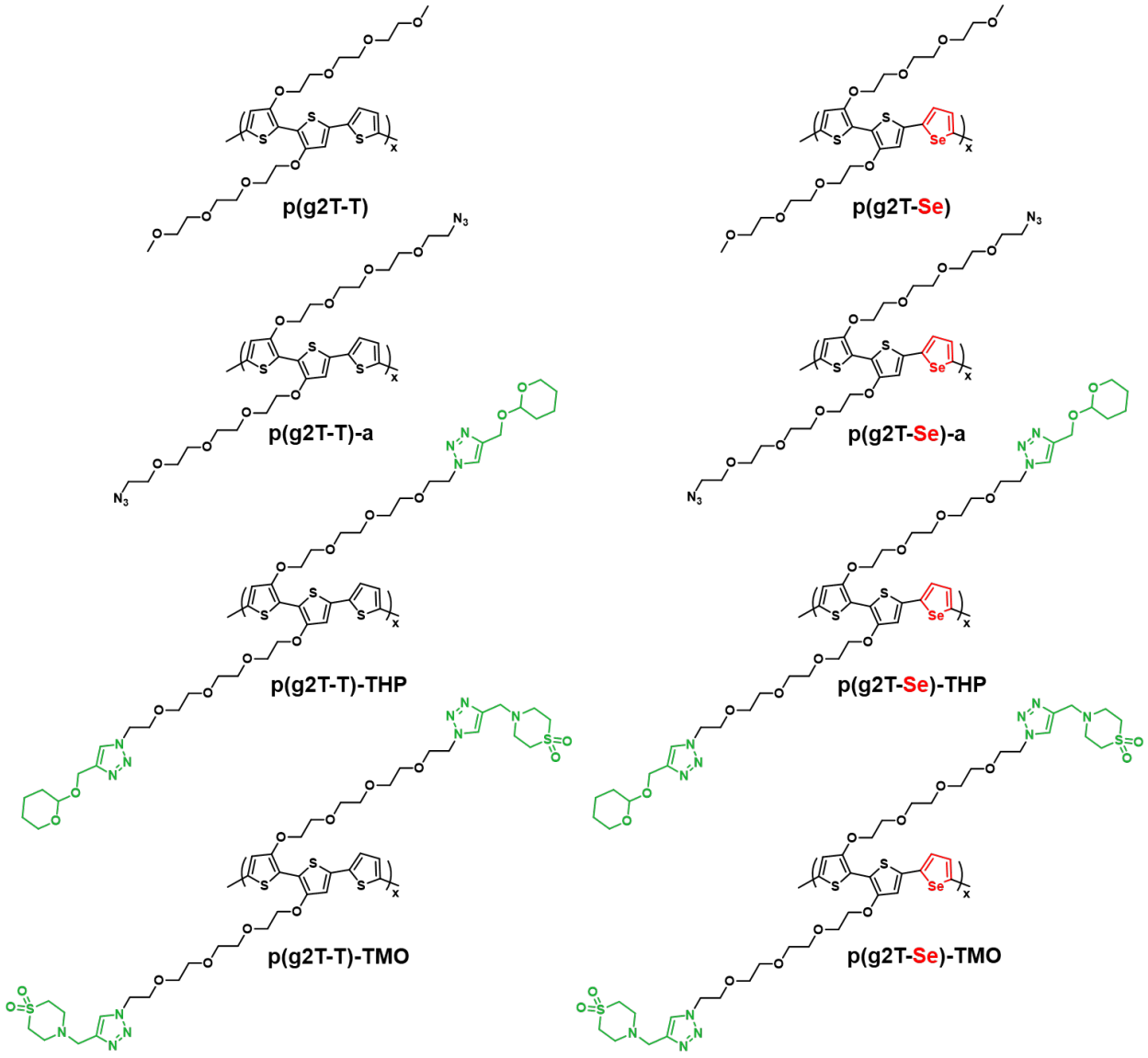

Supplementary Fig. 1 | Chemical structures of the semiconducting polymers investigated in the work. P(g2T-T) and p(g2T-Se) are prepared following previous literature[1].

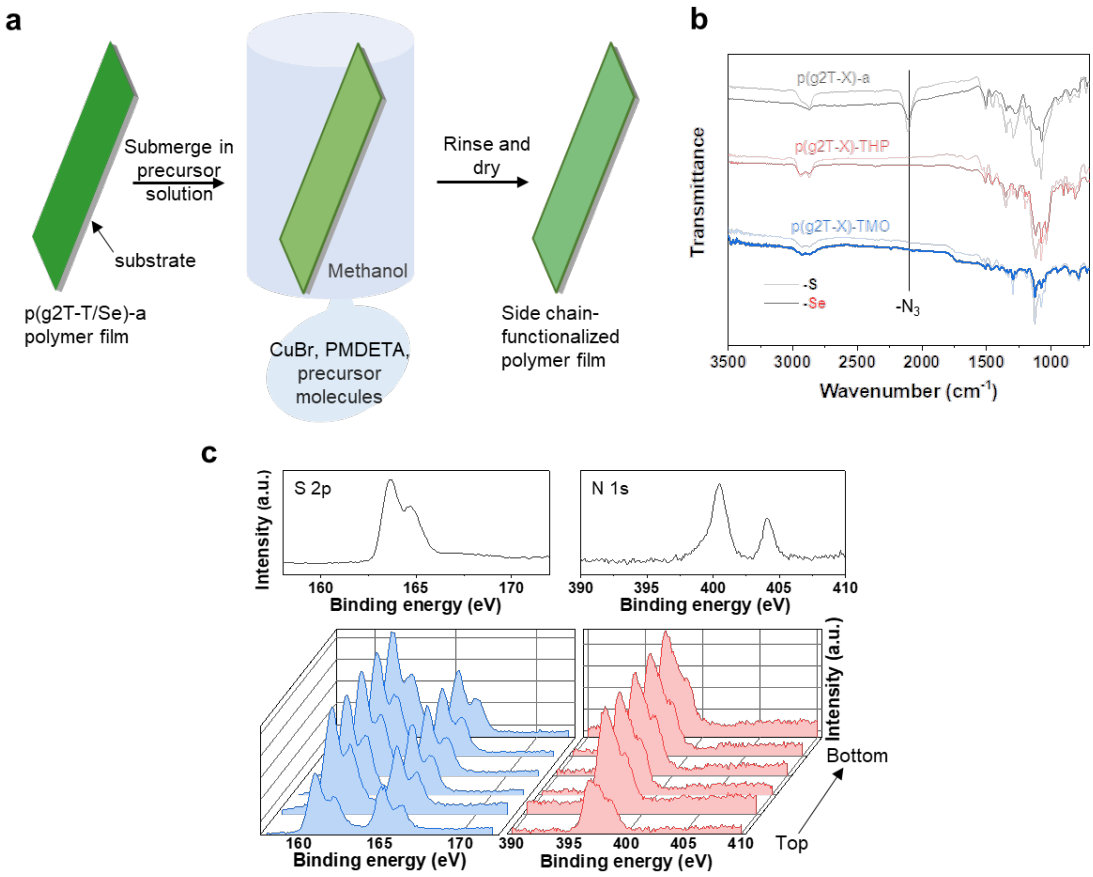

Supplementary Fig. 2 | Side-chain functionalization on semiconducting polymer films using the CLIP method[1]. a, Scheme illustrating the side chain functionalization procedure on semiconducting polymers p(g2T-T)-a and p(g2T-Se)-a. **b**, Fourier-transform infrared (FTIR) spectrum, verifying the disappearance of the azide peak after side chain functionalization. **c**, Depth-profiling XPS spectra showing S 2p and N 1s peaks for p(g2T-T)-a (top) and p(g2T-T)-TMO (bottom).

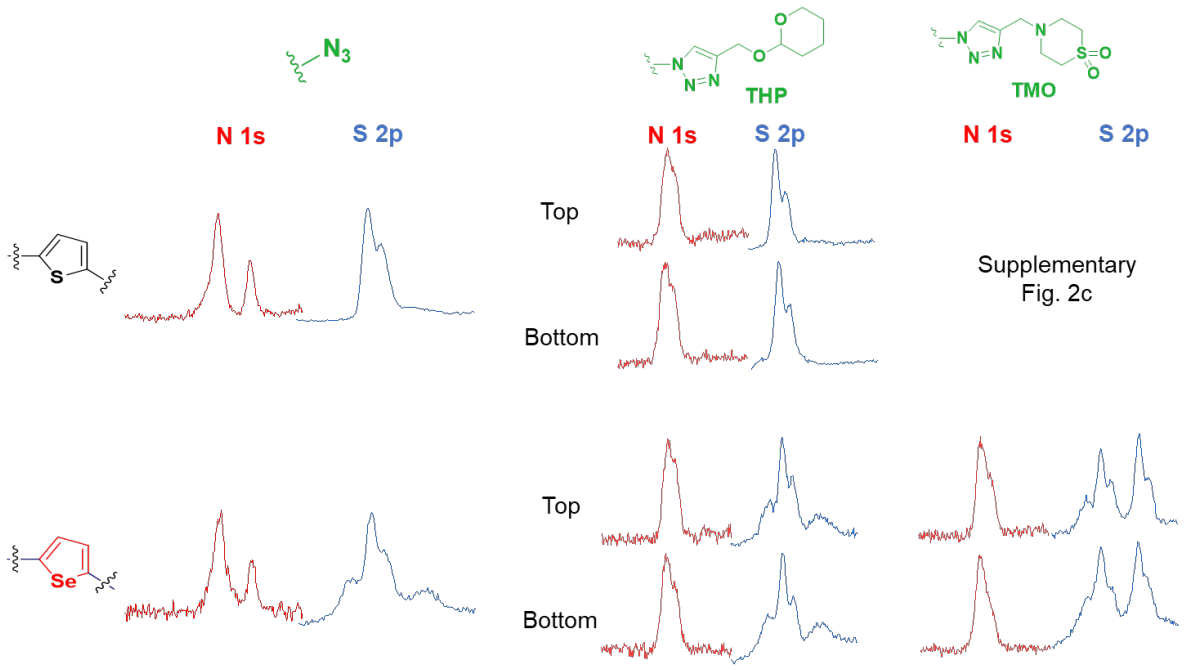

Supplementary Fig. 3 | XPS characterization illustrating N 1s and S 2p peaks on top and bottom surfaces of a film before and after side chain functionalization. The results indicate successful functionalization of THP and TMO groups through the CLIP method in the film.

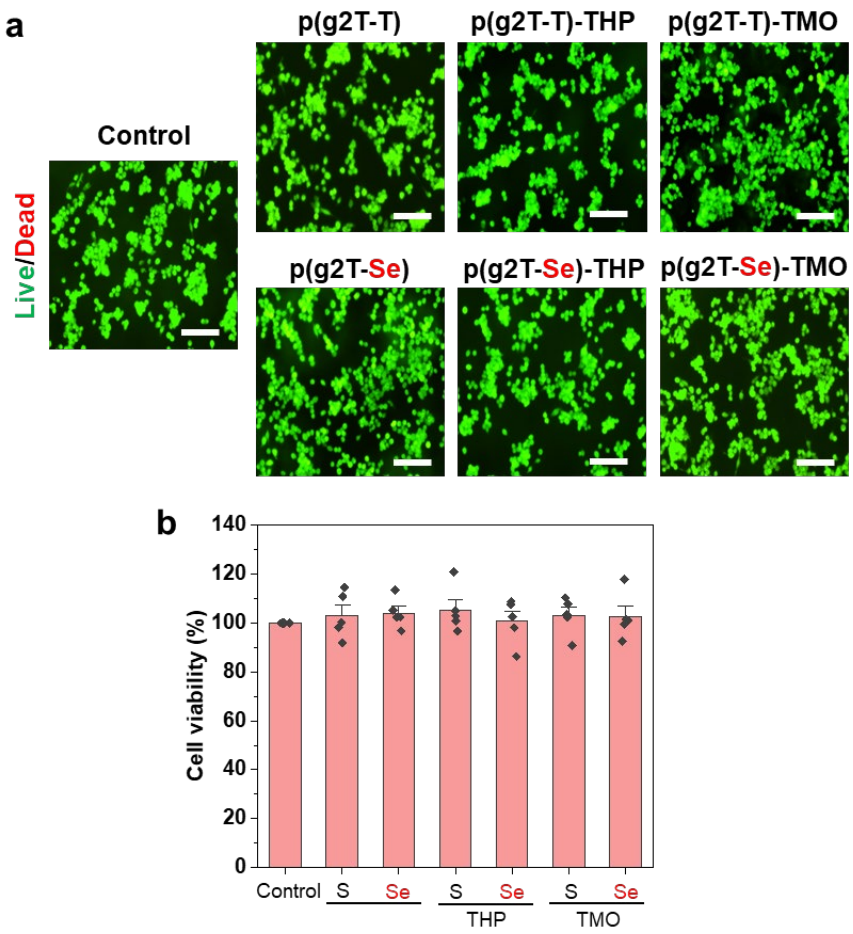

Supplementary Fig. 4 | Cell viability test of the semiconducting polymers that are studied in this work. a, Live/dead test. Scale bars, 200 μm. **b**, MTT assay. Uncoated SEBS substrates were used as the control. Values in **b** represent mean values ± s.e.m. (n = 5 biologically independent samples). All semiconducting polymers do not show significant cell toxicity.

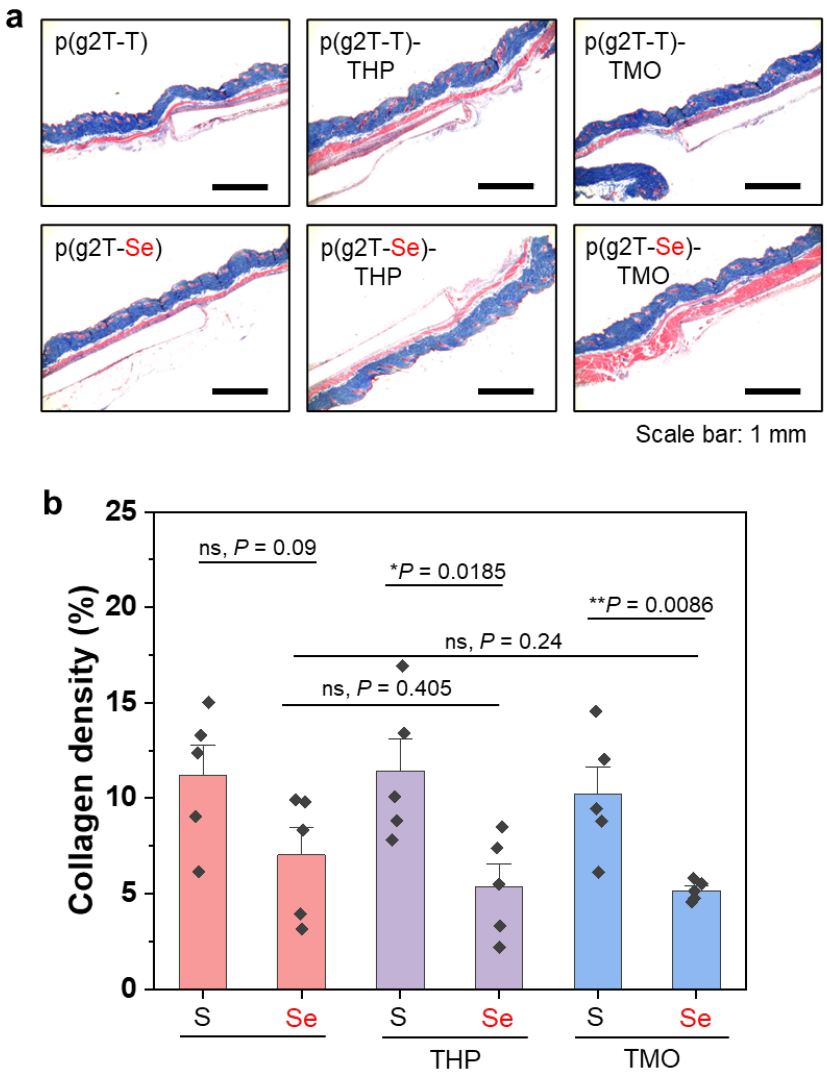

Supplementary Fig. 5 | Masson's trichrome staining (a) and collagen density calculation (b) for 1-week implants. Values in **b** represent mean values ± s.e.m. (n = 5 biologically independent samples). Statistical significance and P values are determined by two-sided Student's t-test: *P<0.05; **P<0.01.

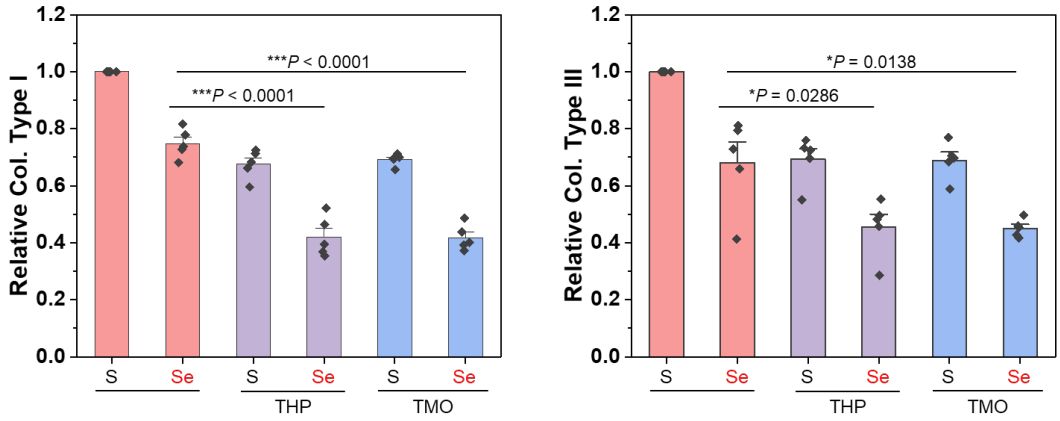

Supplementary Fig. 6 | PCR-based RNA expression levels for collagen types I and III for 1-week implants. The different trends from histological staining and PCR quantification methods for 1-week implants are mainly due to the difference in immune activation and working time points. Collagen mRNA expression is mainly controlled by myofibroblasts or fibroblasts. Normally, these cells are activated in 0~2 weeks after the inflammation signal. But collagen is cross-linked and makes structure after 2 weeks. Values represent mean values ± s.e.m. (n = 5 biologically independent samples). Statistical significance and P values are determined by two-sided Student's t-test: *P<0.05; **P<0.01; ***P<0.001.

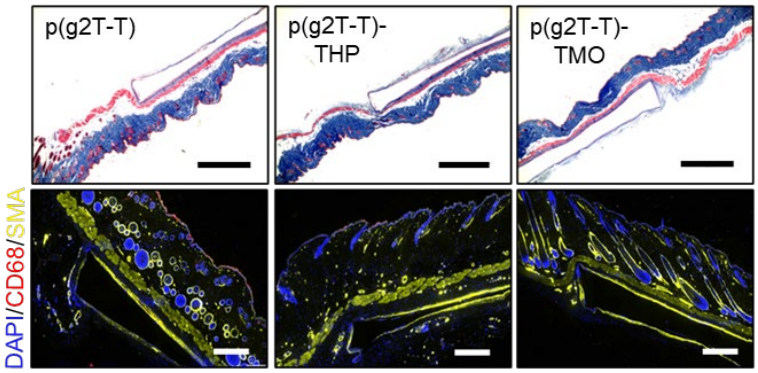

Supplementary Fig. 7 | Staining images from Masson's trichrome and immunofluorescence for p(g2T-T), p(g2T-T)-THP, and p(g2T-T)-TMO polymers. Scale bars, 1 mm for Masson's trichrome staining (top), 500 μm for immunofluorescence staining (bottom). We conducted the replicate experiment twice independently to verify the reproducibility of the experiment and obtained similar results.

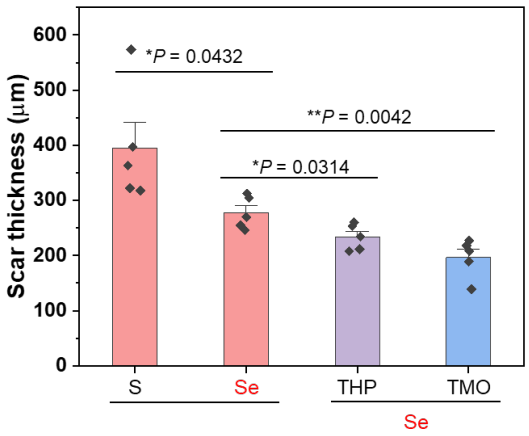

Supplementary Fig. 8 | Scar thickness calculation for 4-week implants. Values represent mean values ± s.e.m. (n = 5 biologically independent samples). Statistical significance and P values are determined by two-sided Student's t-test: *P<0.05; **P<0.01.

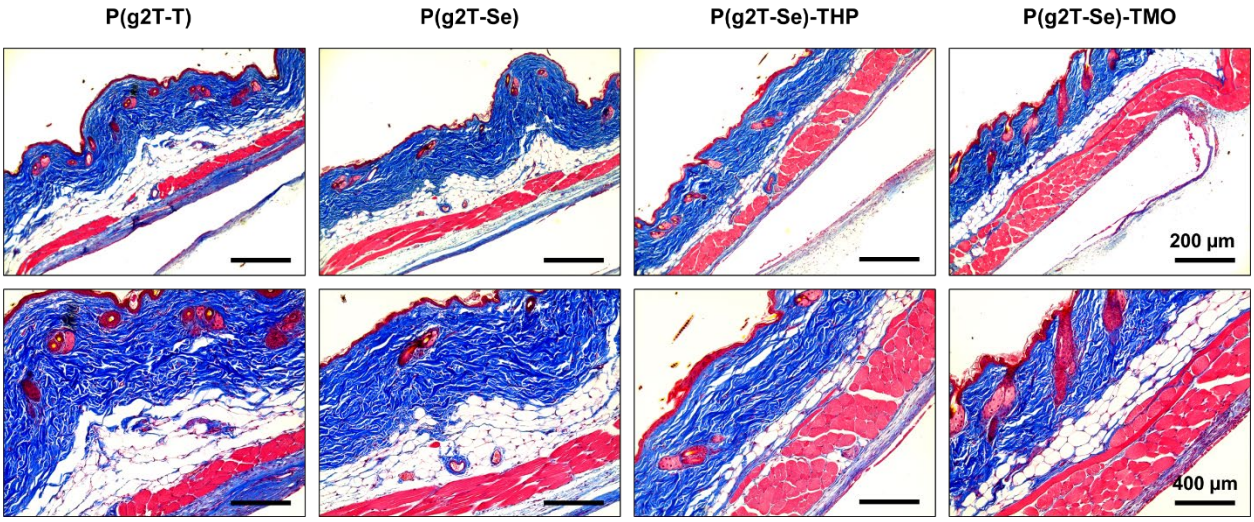

Supplementary Fig. 9 | Skin morphology and thickness of 4-week implants. We conducted the replicate experiment twice independently to verify the reproducibility of the experiment and obtained similar results.

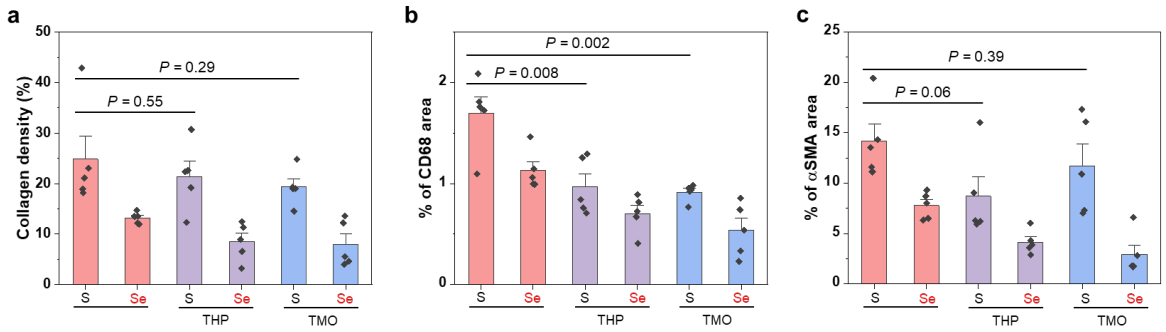

Supplementary Fig. 10 | Collagen deposition and immune-cell populations at the polymer-tissue interface for 4 weeks post-implantation. a, Quantification of collagen density. **b**, CD68 (a marker of macrophages) area. **c**, αSMA (a marker of myofibroblasts) area. Values represent mean values ± s.e.m. (n = 5 biologically independent samples). Statistical significance and P values are determined by two-sided Student's t-tests.

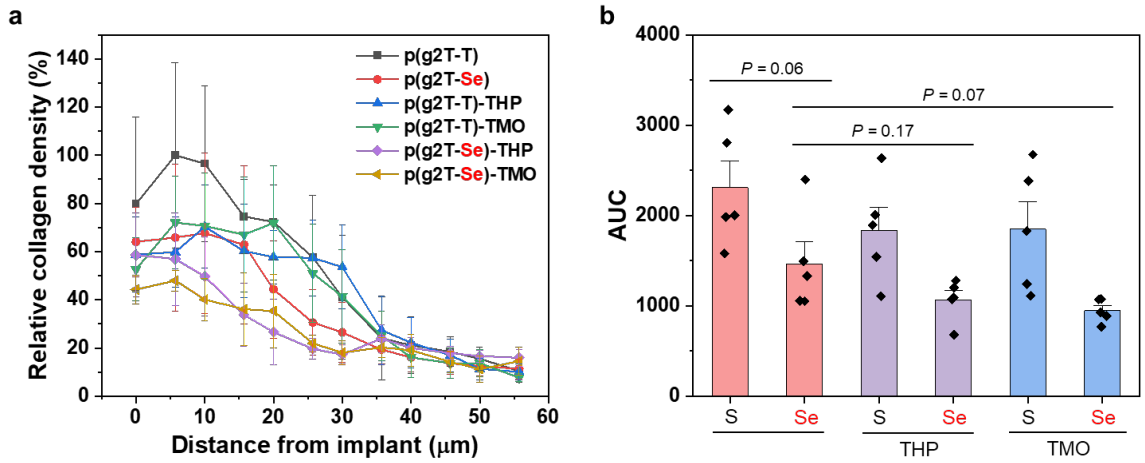

Supplementary Fig. 11 | Quantification of collagen density (a) as a function of the distance from the implant surface to the tissue surface and the area under the curve (AUC) (b). Values represent mean values ± s.e.m. (n = 5 biologically independent samples). Statistical significance and P values are determined by two-sided Student's t-tests.

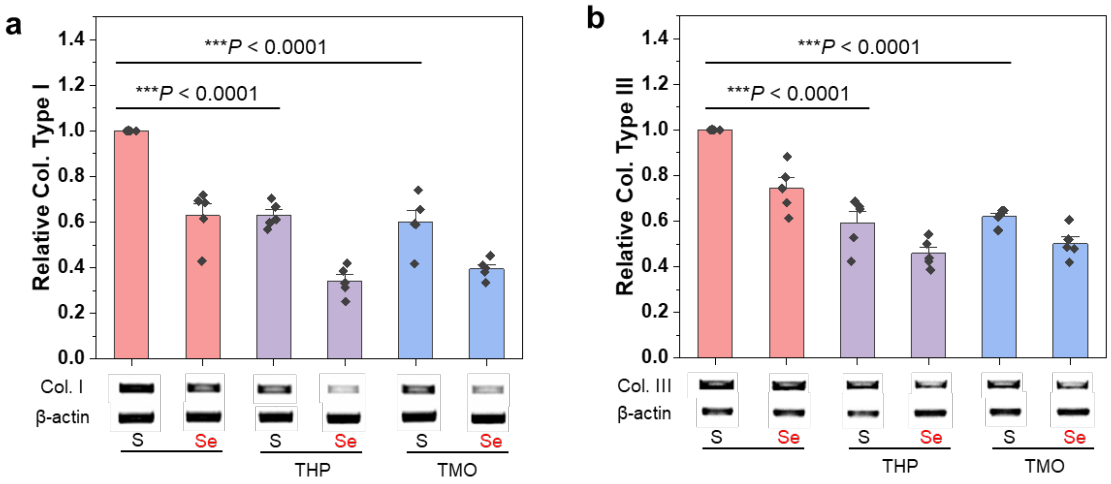

Supplementary Fig. 12 | Analysis of collagen expression at the semiconducting polymer-tissue interface. a, **b**, Relative Col. Type I (**a**) and Col. Type III (**b**) mRNA expression level (fold change) in the implanted region. Values represent mean values ± s.e.m. (n = 5 biologically independent samples). Statistical significance and P values are determined by two-sided Student's t-tests: ***P<0.001. Side chain functionalization with THP and TMO groups significantly decreases the expression level of Col. Type I and Col. Type III on p(g2T-T) polymer.

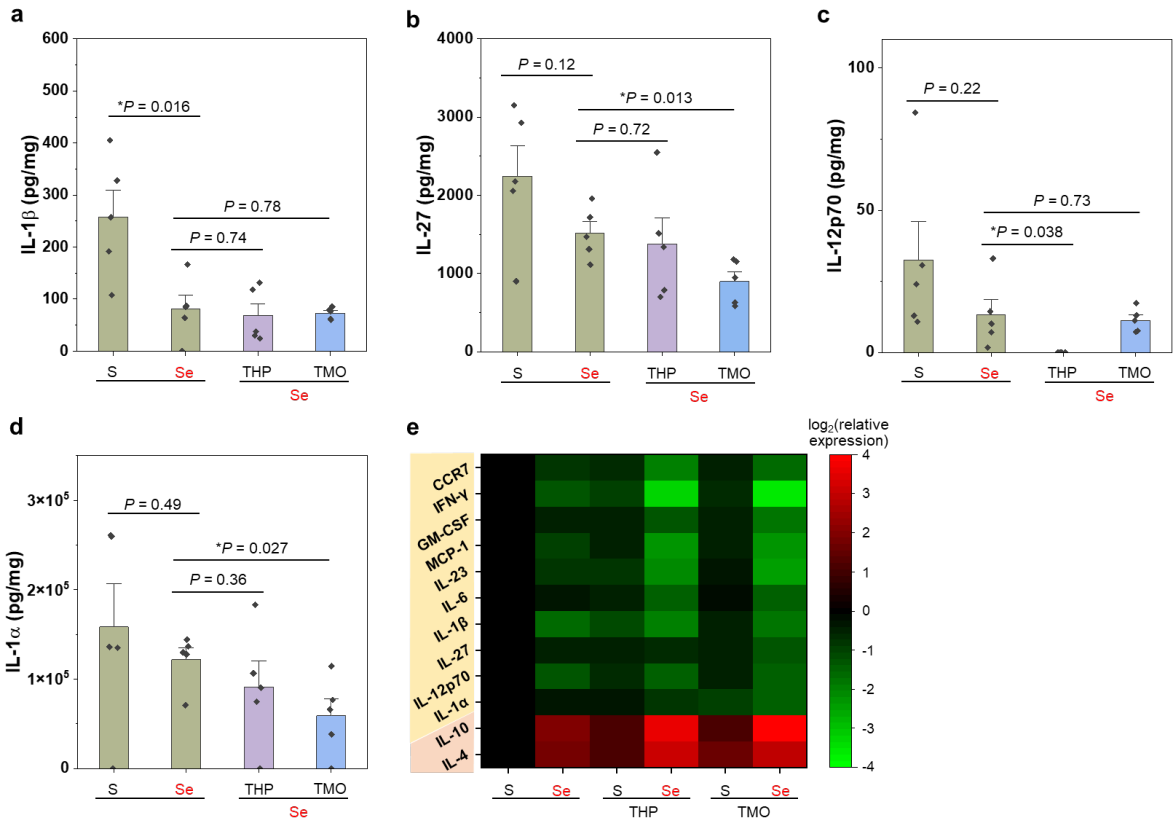

Supplementary Fig. 13 | Additional cytokines measured at the semiconducting polymer-tissue interface. a-d, Pro-inflammatory cytokines IL-1β (**a**), IL-27 (**b**), IL-12p70 (**c**), and IL-1α (**d**) expression levels. Values in **a-d** represent mean values ± s.e.m. ($n = 5$ biologically independent samples). Statistical significance and P values are determined by two-sided Student's t-tests: *P<0.05. **e**, Heat map summarizing inflammation-related biomarkers expression level for all semiconducting polymers. Values in **e** represent normalized mean values ($n = 5$ biologically independent samples).

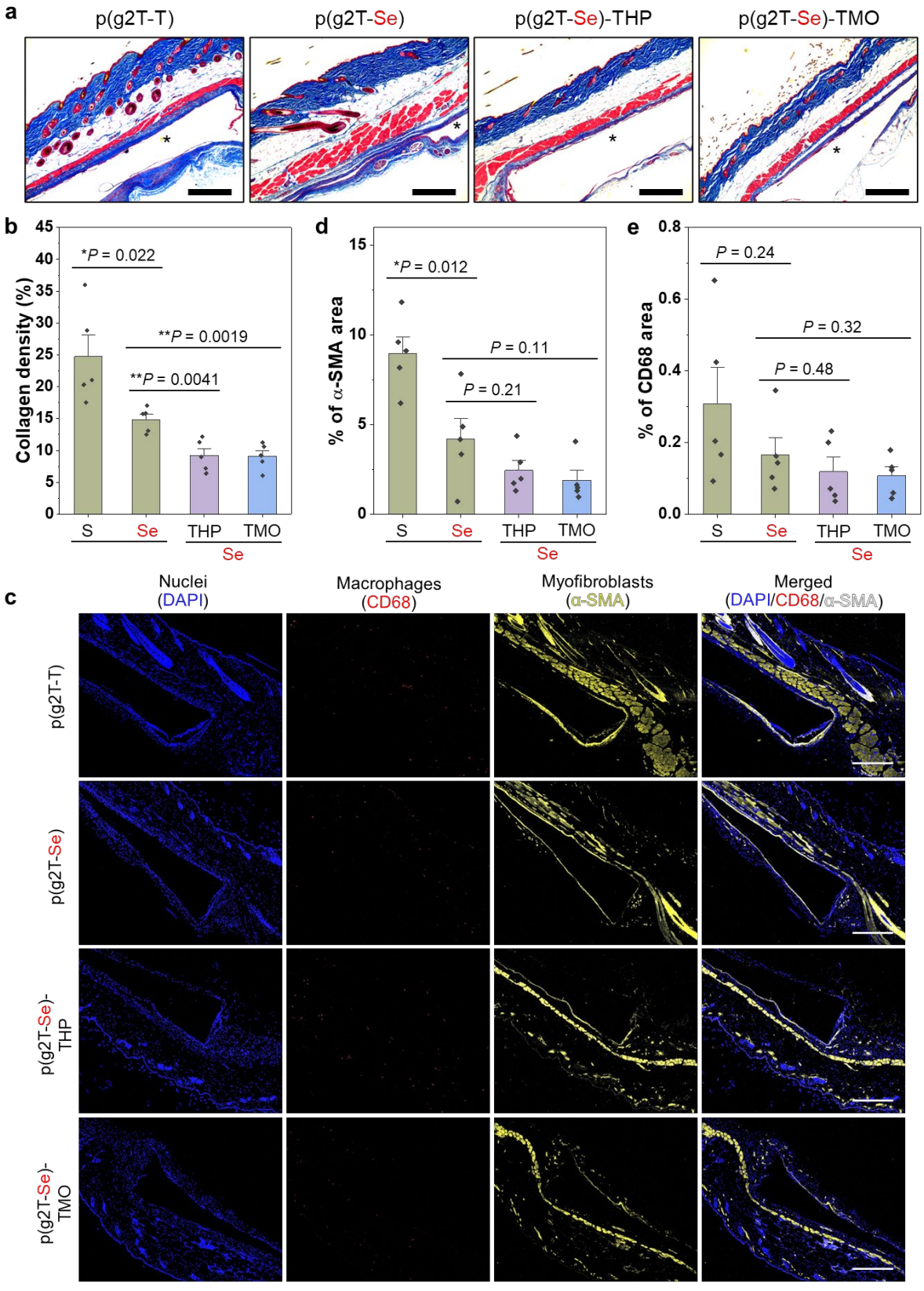
a
p(g2T-T)
p(g2T-Se)
p(g2T-Se)-THP
p(g2T-Se)-TMO
b
Collagen density (%)
*P = 0.022
**P = 0.0019
**P = 0.0041
S
Se
THP
TMO
Se
d
% of α-SMA area
*P = 0.012
P = 0.11
P = 0.21
S
Se
THP
TMO
Se
e
% of CD68 area
P = 0.24
P = 0.32
P = 0.48
S
Se
THP
TMO
Se
c
Nuclei (DAPI)
Macrophages (CD68)
Myofibroblasts (α-SMA)
Merged (DAPI/CD68/α-SMA)
p(g2T-T)
p(g2T-Se)
p(g2T-Se)-THP
p(g2T-Se)-TMO

Supplementary Fig. 14 | Reduced collagen deposition on the polymer films with immune-compatible designs for 3-month implantation. **a**, Masson's trichrome-stained tissue sections of p(g2T-T), p(g2T-Se), p(g2T-Se)-THP, and p(g2T-Se)-TMO polymers after 3-month subcutaneous implantation. The asterisk (*) indicates the implant locations. Scare bars, 1 mm. **b**, Extracted collagen densities showing decreased collagen deposition from the selenophene backbone and immunomodulatory side-chain engineering. **c**, Immunofluorescence images showing cell nuclei (DAPI; blue), macrophages (CD68; red), and myofibroblasts (α-SMA; yellow) for the four polymers. Scale bars, 500 μm. **d**, **e**, Quantification of α-SMA (**d**) and CD68 (**e**) area at the tissue-polymer interface in the immunofluorescence images. Values in **b**, **d**-**e** represent mean values ± s.e.m. (n = 5 biologically independent samples). Statistical significance and P values are determined by two-sided Student's t-test: *P<0.05; **P<0.01.

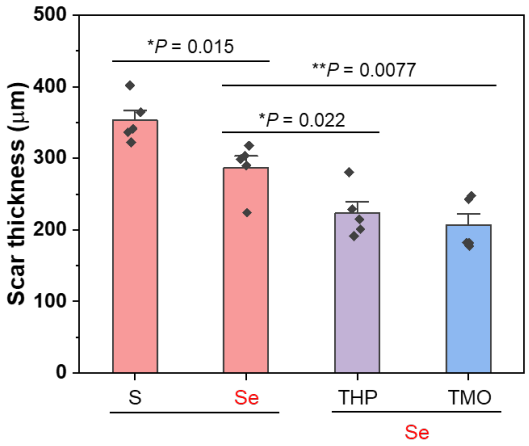

Supplementary Fig. 15 | Scar thickness of the 3-month implantation groups. Values represent mean values ± s.e.m. (n = 5 biologically independent samples). Statistical significance and P values are determined by two-sided Student's t-test: *P<0.05; **P<0.01.

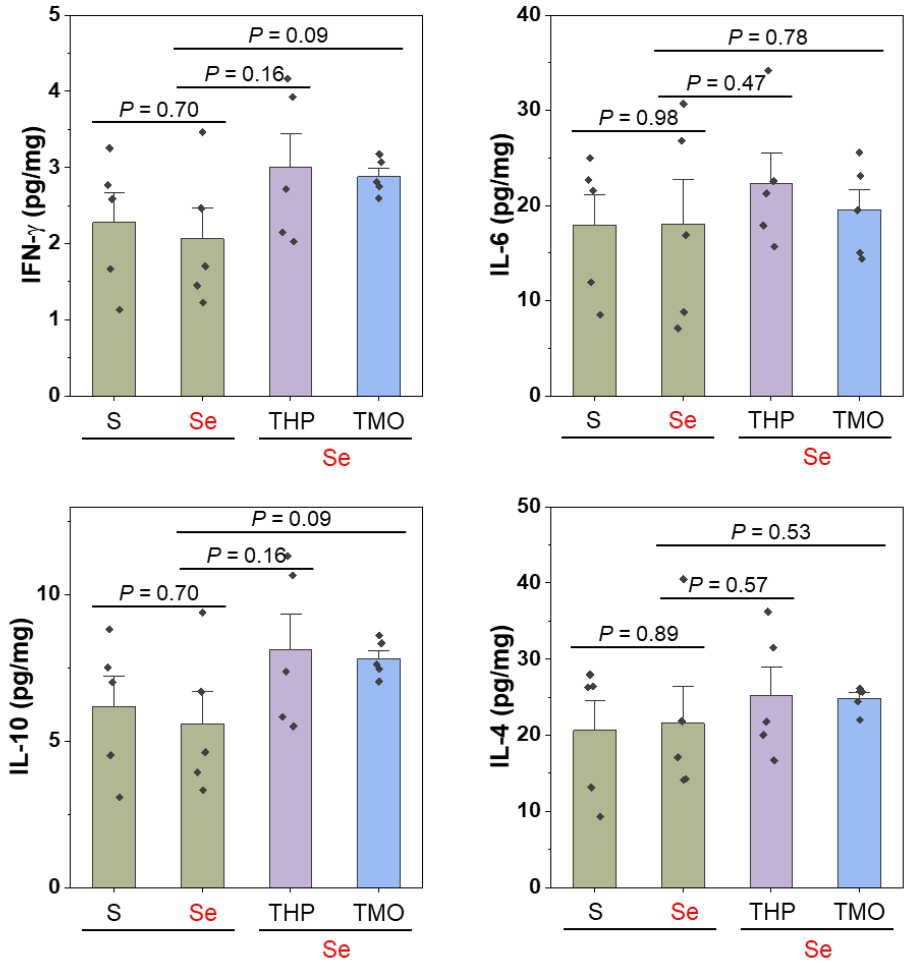

Supplementary Fig. 16 | Expression levels of representative inflammatory makers (IFN-γ, IL-6, IL-10, IL-4) for 3-month implantation. Values represent mean values ± s.e.m. (n = 5 biologically independent samples). Statistical significance and P values are determined by two-sided Student's t-test.

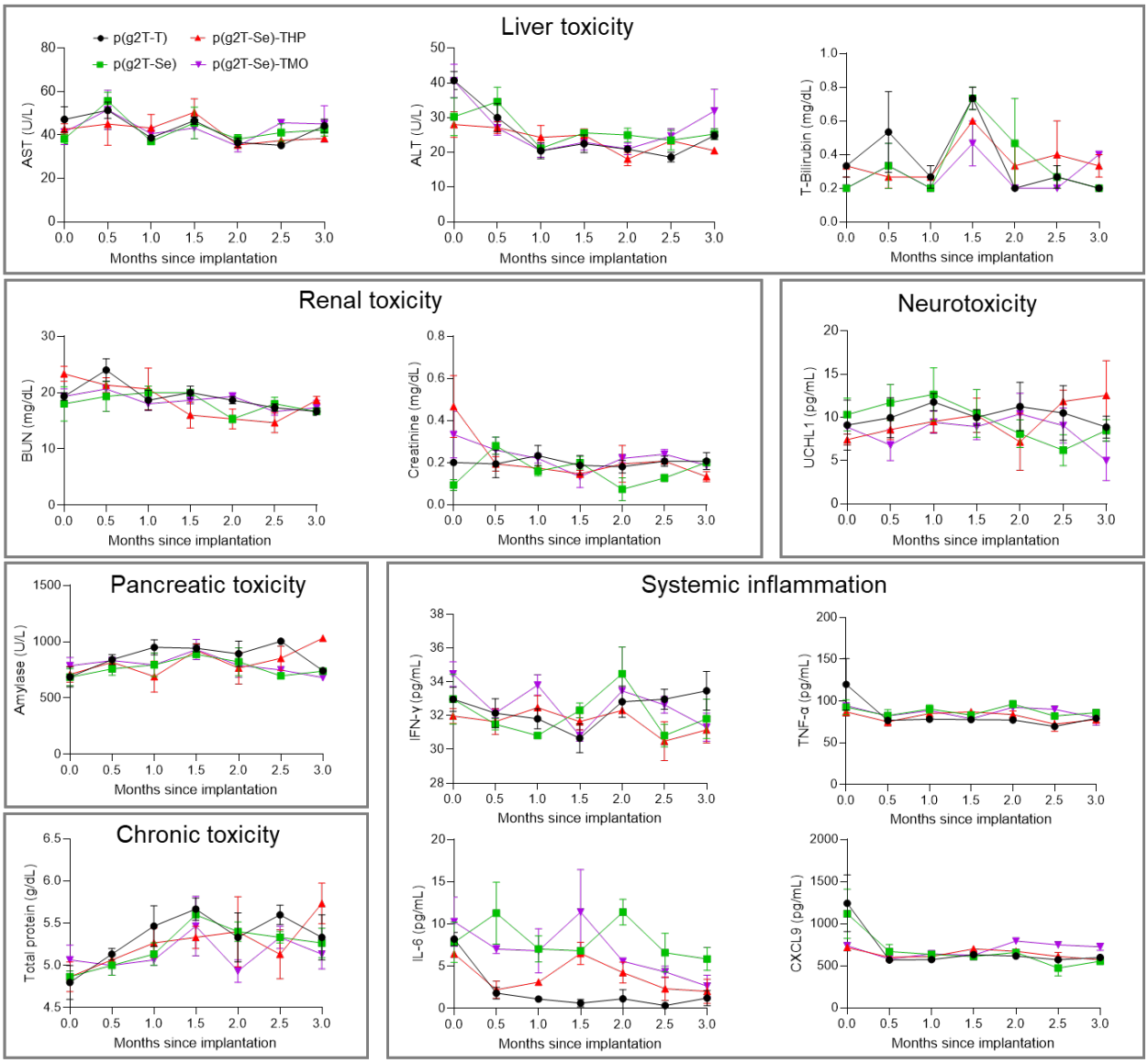

Supplementary Fig. 17 | Blood toxicity test at different time points post-implantation. A range of biomarkers, including those of liver, renal, neuro-, pancreatic, and chronic toxicities, as well as systemic inflammation, were tested. Values represent mean values ± s.d. (n = 5 biologically independent samples).

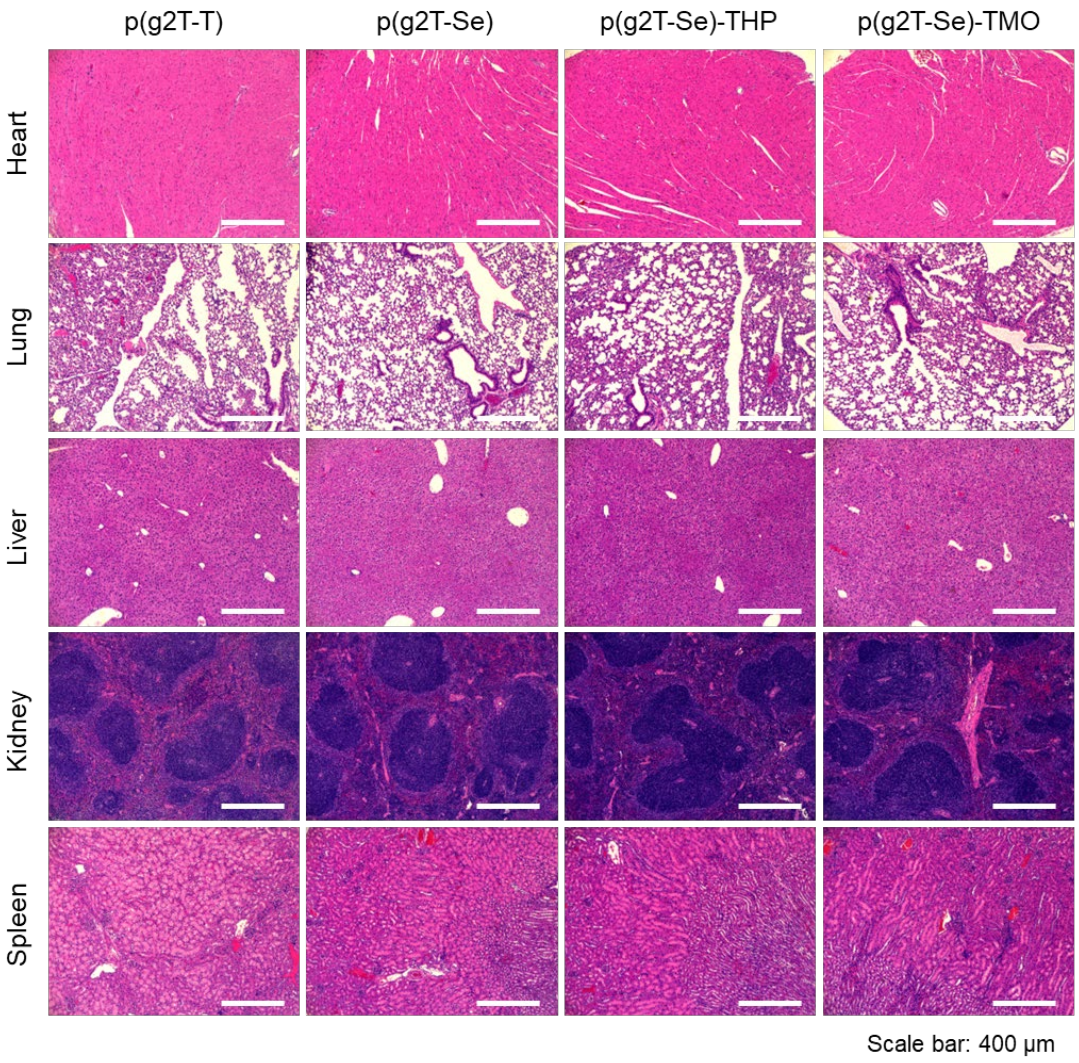

Supplementary Fig. 18 | Hematoxylin and eosin staining images of major organs (heart, lung, liver, kidney, spleen) post 3-month implantation. We conducted the replicate experiment twice independently to verify the reproducibility of the experiment and obtained similar results.

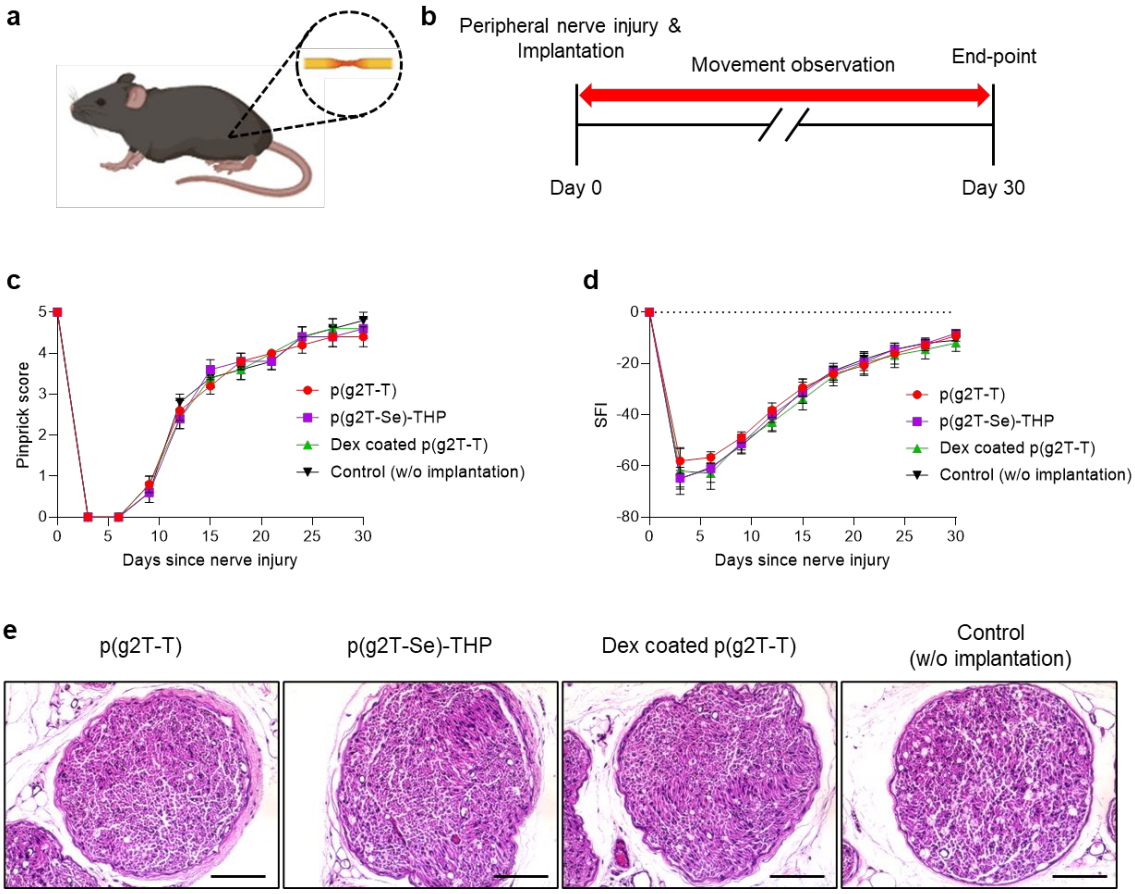

Supplementary Fig. 19 | Influence of semiconducting polymers on peripheral nerve regeneration. a, Schematic illustrating the peripheral nerve injured mouse. **b**, Experimental schedule. **c**, **d**, Pinprick scores (**c**) and sciatic function index (SFI, **d**) for monitoring nerve functionality and recovery from nerve injury for implants of p(g2T-T), p(g2T-Se)-THP, dexamethasone (Dex)-coated p(g2T-T), and control group (without implantation). **e**, H&E staining results for the nerve tissue at day 30 since the injury. Scale bars, 100 μm. Values in **c-d** represent mean values ± s.d. (n = 5 biologically independent samples).

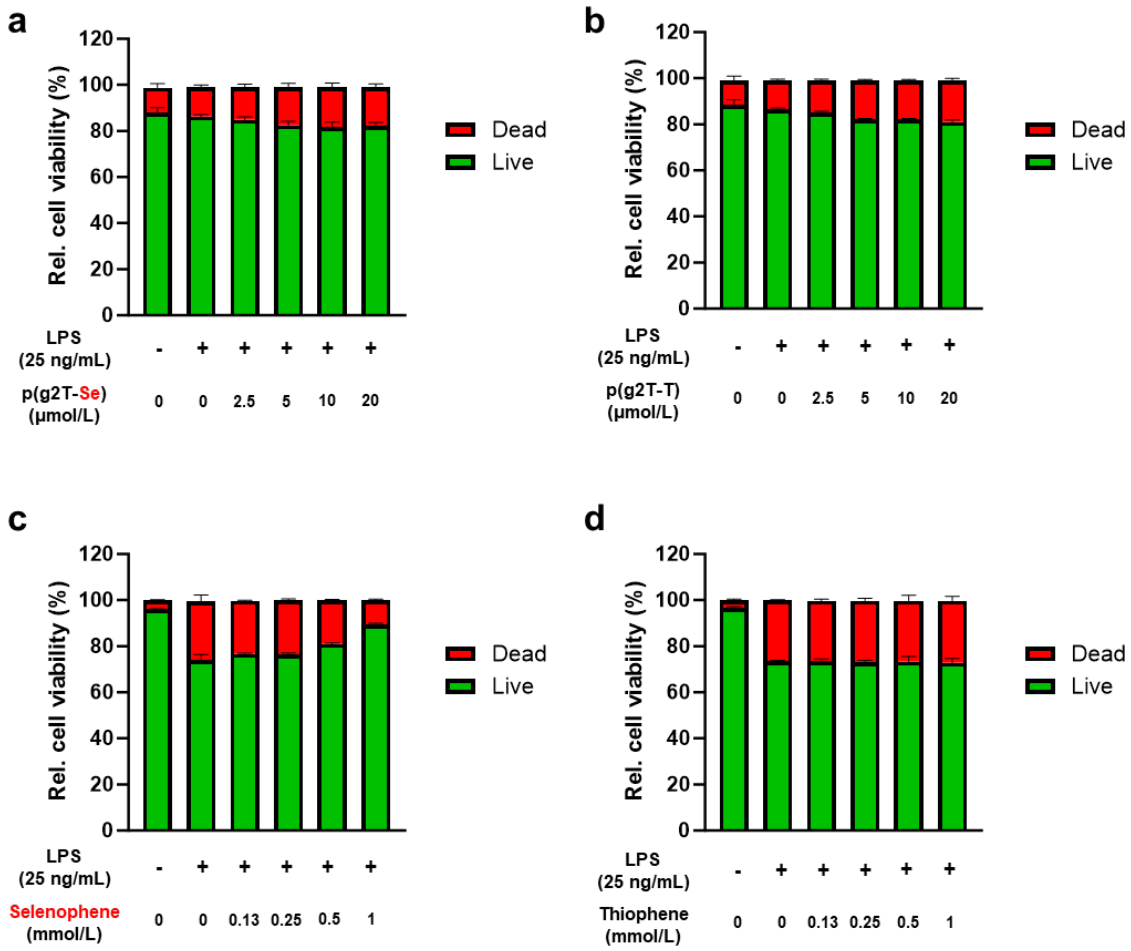

Supplementary Fig. 20 | Study of cell toxicity of p(g2T-Se) (a), p(g2T-T) (b), selenophene (c), and thiophene (d) during in vitro cell treatment. Values represent mean values ± s.e.m. (n = 5 biologically independent samples).

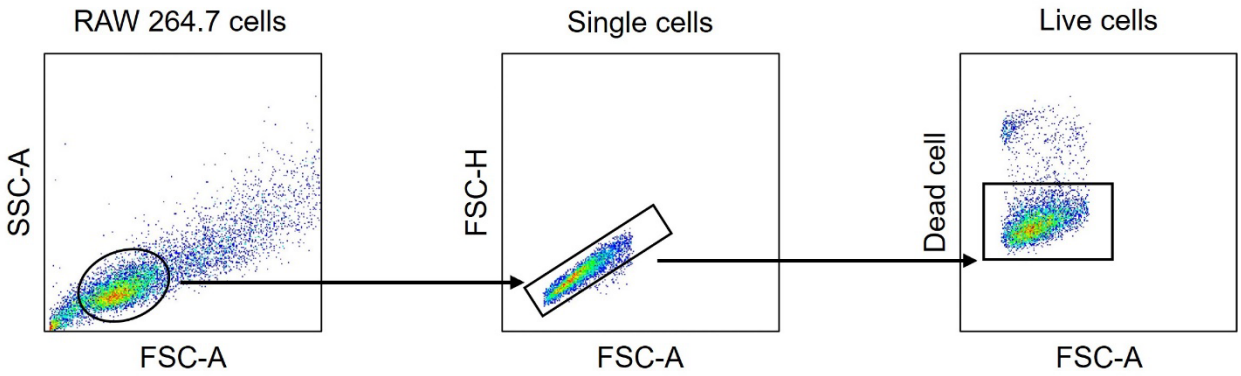

Supplementary Fig. 21 | Flow gating of intracellular inflammatory proteins in RAW 264.7 cells including p-p38, p-ERK, iNOS, and p-JNK. The gating strategy shows the single-cell data editing process. Side scattering (SSC) and forward scattering (FSC) data show cell density and morphology. Cells with similar structure (i.e., similar density and morphology) were collected. FSC-H and FSC-A both are forward scattering data. Single cells show similar FSC-H and FSC-A, but aggregated cells (dimer, trimer....) show some differences in pattern. Here, single cells (with similar FSC-H and FSC-A) were collected. Dead cell staining (only dead cells) was done to check the polymer's cell viability. Dead cells (stained cells) are placed on the upper side of the figure and live cells (unstained cells) are placed on the bottom side. And the expression level of inflammatory protein markers was analyzed using only these live cells.

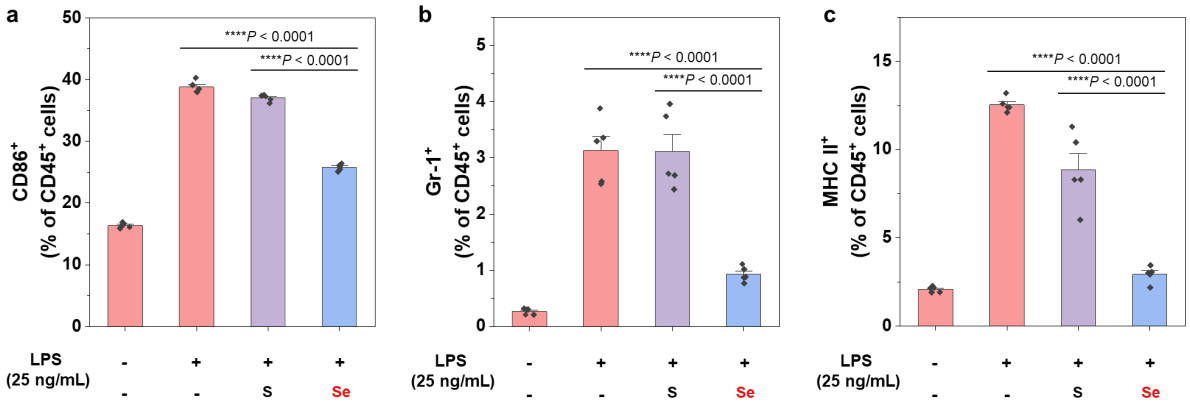

Supplementary Fig. 22 | In vitro quantification of pro-inflammatory markers on macrophages, which reflect the amount of M1 macrophages. a-c, The expression levels of $CD86^+$ (**a**), $Gr\text{-}1^+$ (**b**), and $MHC\text{-}II^+$ (**c**) after being treated with the thiophene (S) and selenophene (Se) monomers, respectively. Values represent mean values ± s.e.m. (n = 5 biologically independent samples). Statistical significance and P values are determined by ordinary one-way ANOVA: ****P<0.0001.

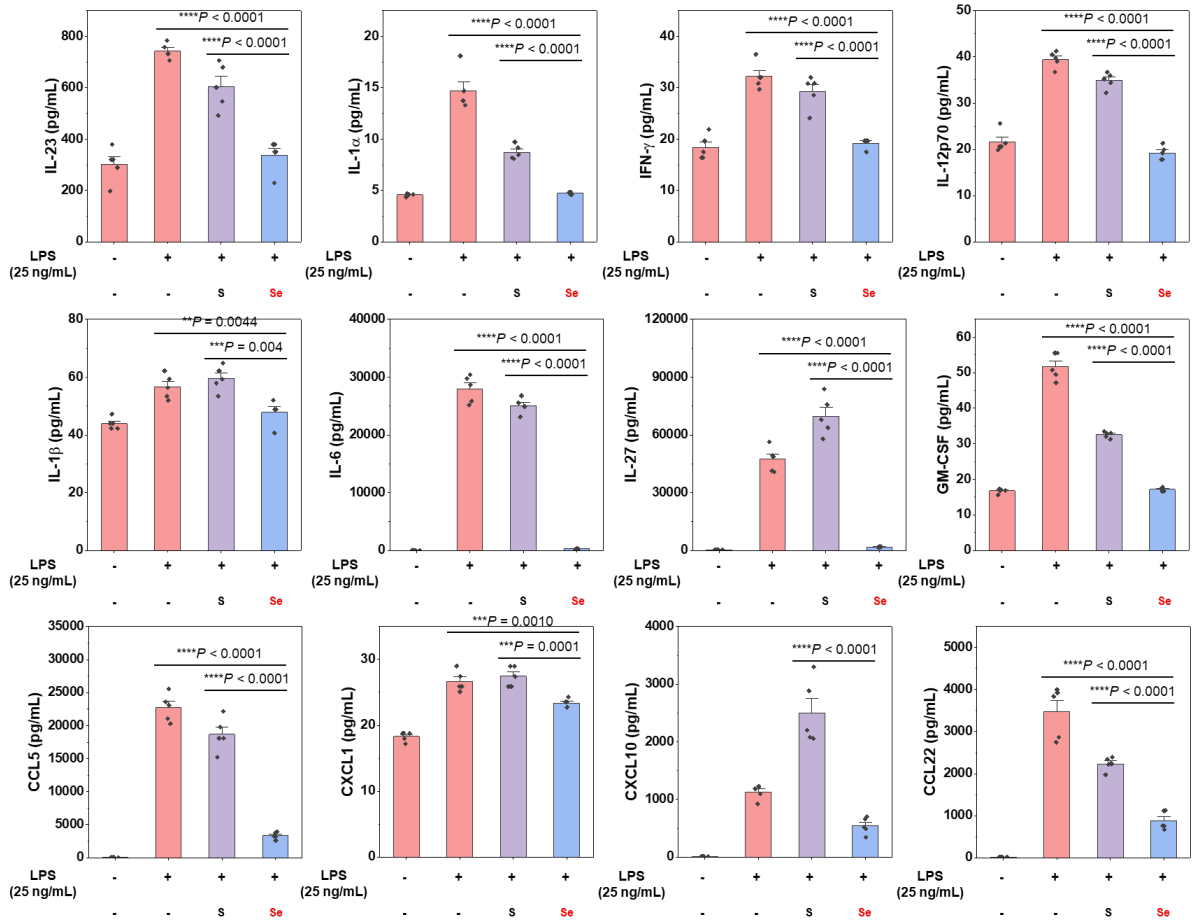

Supplementary Fig. 23 | In vitro measurement of pro-inflammatory cytokines or chemokines levels in cell supernatant after being treated with thiophene and selenophene monomers, respectively. Values represent mean values ± s.e.m. (n = 5 biologically independent samples). Statistical significance and P values are determined by ordinary one-way ANOVA: $^{**}P<0.01$; $^{***}P<0.001$; $^{****}P<0.0001$.

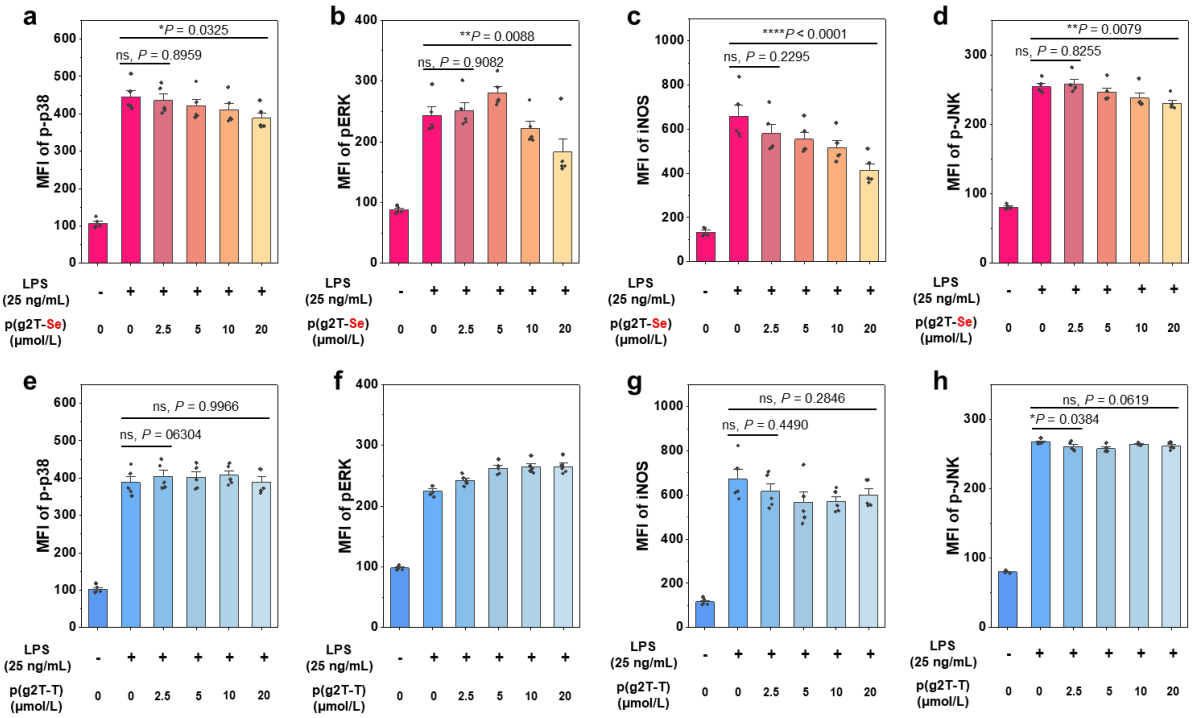

Supplementary Fig. 24 | *In vitro* study of the inhibitory effects of p(g2T-Se) and p(g2T-T) on inflammatory responses. a-d, MFI of different inflammation-related biomarkers p-p38 (**a**), p-ERK (**b**), iNOS (**c**), and p-JNK (**d**) under the exposure of p(g2T-Se). **e-h**, MFI of different inflammation-related biomarkers p-p38 (**e**), p-ERK (**f**), iNOS (**g**), and p-JNK (**h**) under the exposure of p(g2T-T). Values represent mean values ± s.e.m. (n = 5 biologically independent samples). Statistical significance and P values are determined by ordinary one-way ANOVA: *P<0.05; **P<0.01; ***P<0.001; ****P<0.0001; ns, not significant. P(g2T-Se) showed suppressed expression of the biomarkers especially pERK and iNOS in a dose-dependent way, while p(g2T-T) had no such effect.

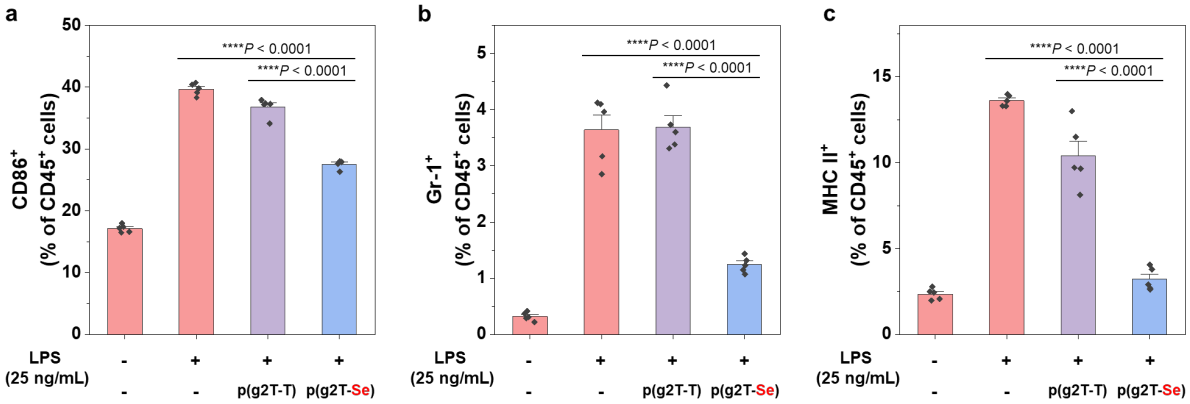

Supplementary Fig. 25 | In vitro quantification of pro-inflammatory markers on macrophages, which reflect the amount of M1 macrophages. a-c, The expression levels of $CD86^+$ (**a**), $Gr\text{-}1^+$ (**b**), and $MHC\text{-}II^+$ (**c**) after being treated with the p(g2T-T) and p(g2T-Se) polymers, respectively. Values represent mean values ± s.e.m. (n = 5 biologically independent samples). Statistical significance and P values are determined by ordinary one-way ANOVA: ****P<0.0001.

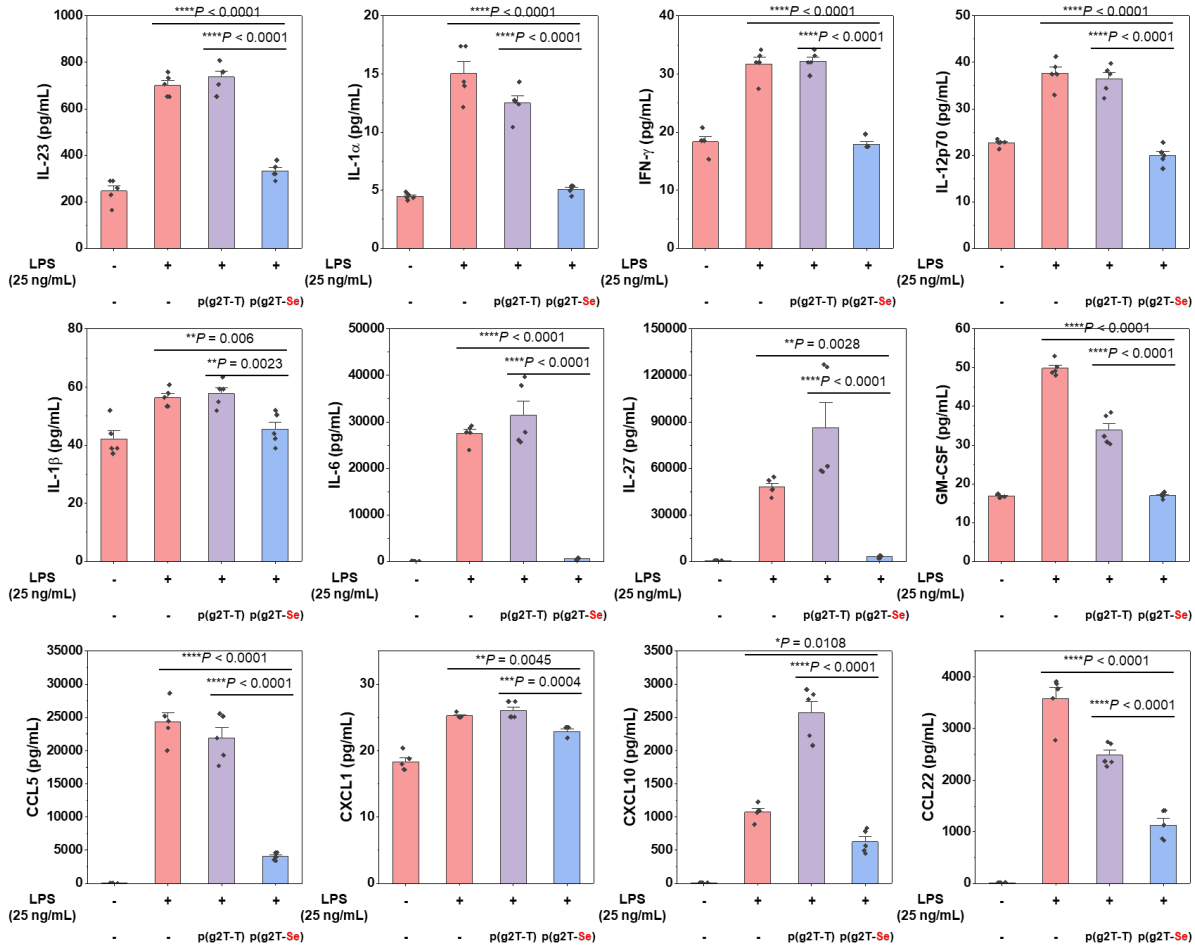

Supplementary Fig. 26 | In vitro measurement of pro-inflammatory cytokines or chemokines levels in cell supernatant after being treated with p(g2T-T) and p(g2T-Se), respectively. Values represent mean values ± s.e.m. (n = 5 biologically independent samples). Statistical significance and P values are determined by ordinary one-way ANOVA: *P<0.05; **P<0.01; ***P<0.001; ****P<0.0001.

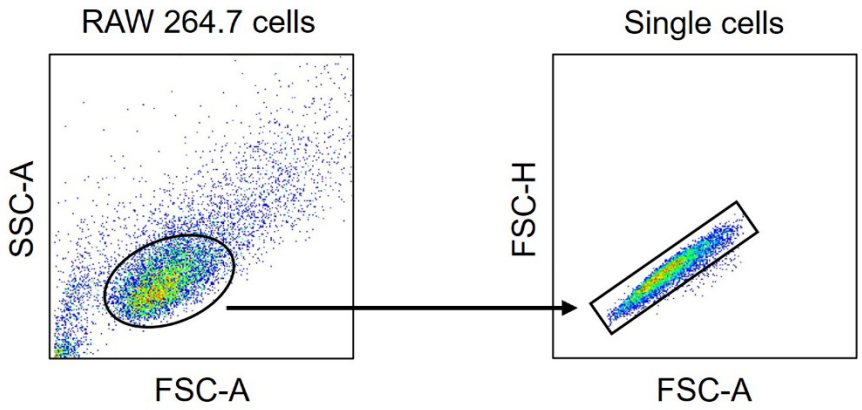

Supplementary Fig. 27 | Flow gating of intracellular reactive oxygen species in RAW 264.7 cells using $DCFH_2$-DA.

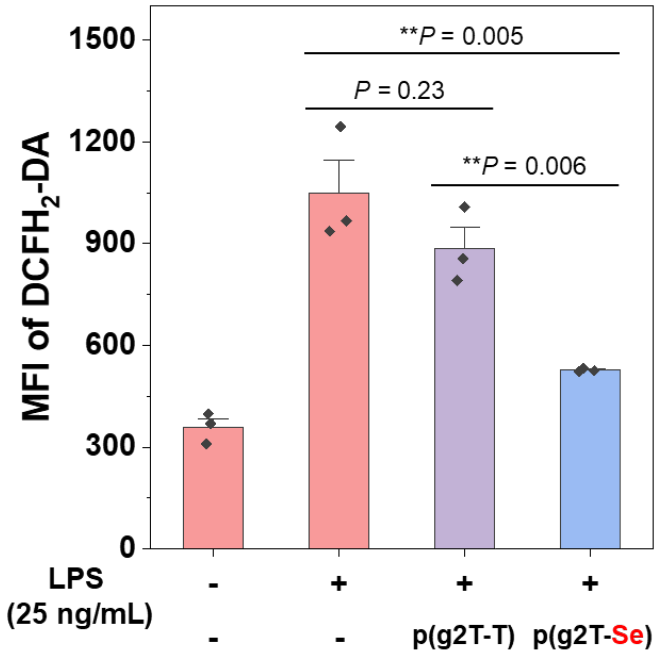

Supplementary Fig. 28 | ROS levels after treatment with p(g2T-T) and p(g2T-Se) polymers. Values represent mean values ± s.e.m. (n = 3 biologically independent samples). Statistical significance and P values are determined by two-sided Student's t-tests: $^{**}P<0.01$. Compared to p(g2T-T), p(g2T-Se) polymer treatment led to a more substantial decrease of ROS level.

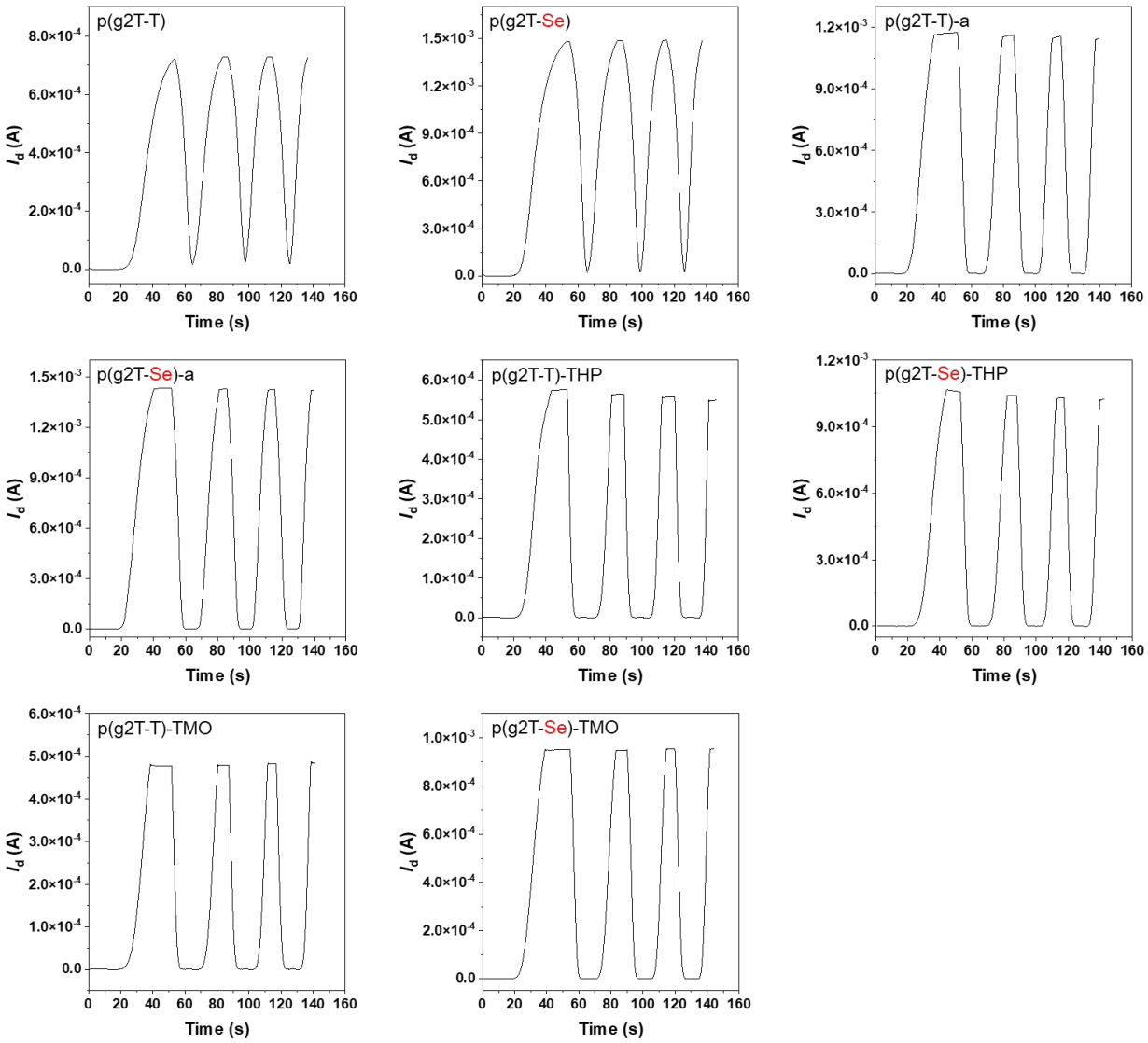

Supplementary Fig. 29 | Absolute drain current responses from constant gate current method for charge carrier mobility measurement.

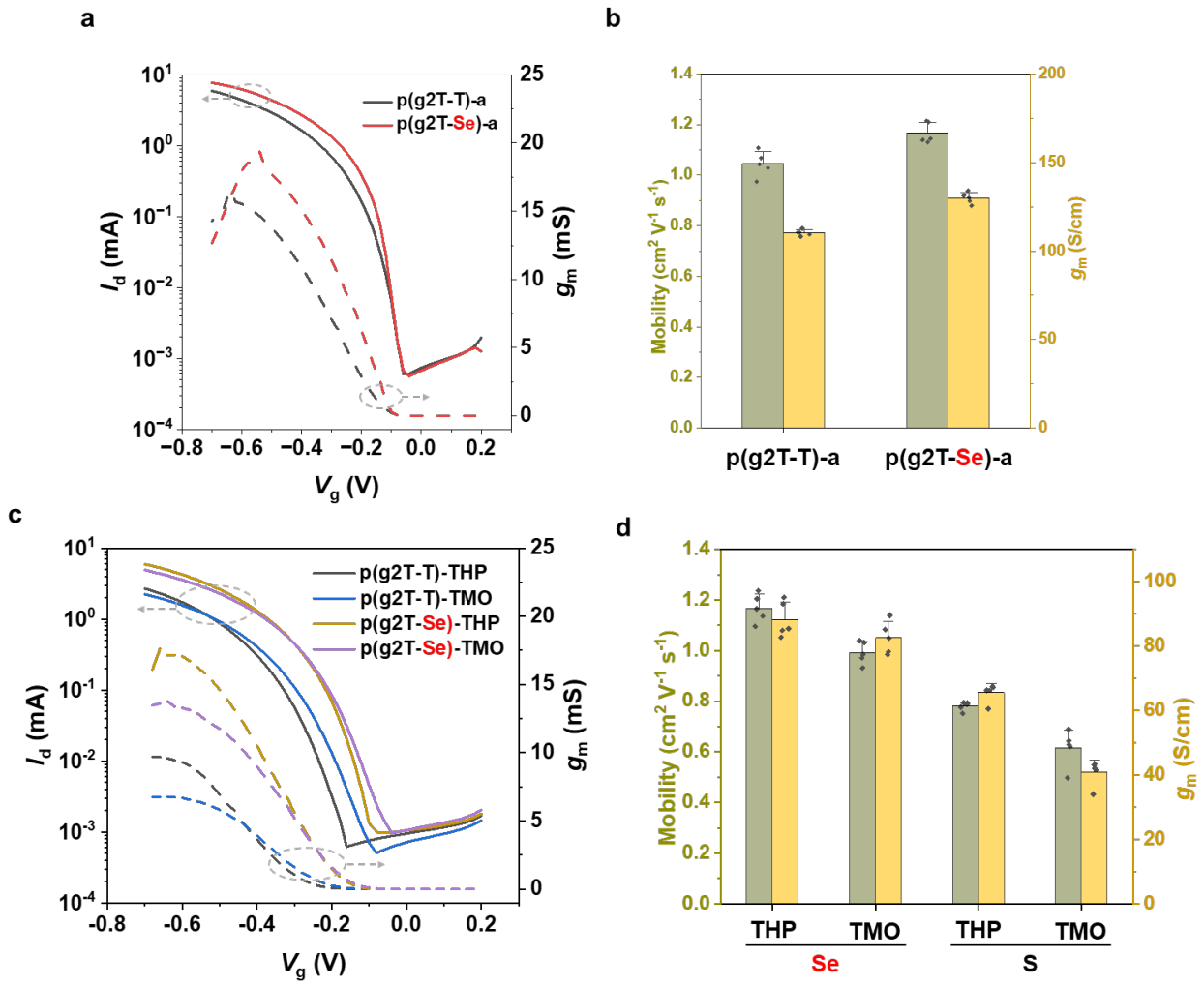

Supplementary Fig. 30 | OECT characterization for p(g2T-T)-a, p(g2T-Se)-a, and side chain functionalized polymers. **a**, **b**, Transfer characteristics (**a**), mobility and normalized transconductance (**b**) for p(g2T-T)-a and p(g2T-Se)-a. **c**, **d**, Transfer characteristics (**c**), mobility and normalized transconductance (**d**) for side-chain functionalized polymers. Values in **b** and **d** represent mean values ± s.d. (n = 5 individual channels).

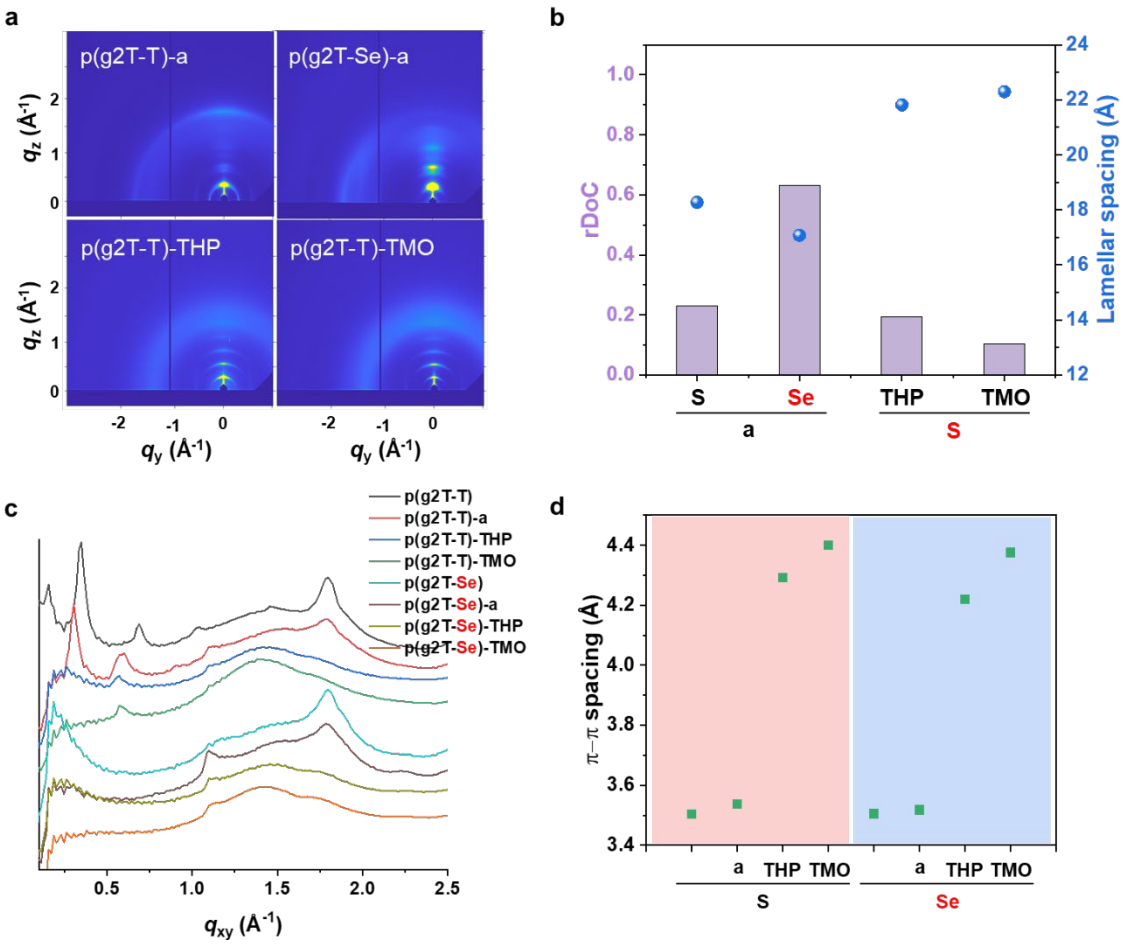

Supplementary Fig. 31 | GIXD characterization of side-chain functionalization. a, **b**, 2D GIXD images (**a**), rDoC and lamellar spacing (**b**) of p(g2T-T)-a, p(g2T-Se)-a, p(g2T-T)-THP and p(g2T-T)-TMO. **c**, **d**, In-plane 1D linecut (**c**) and π-π spacing (**d**) for all semiconducting polymers.

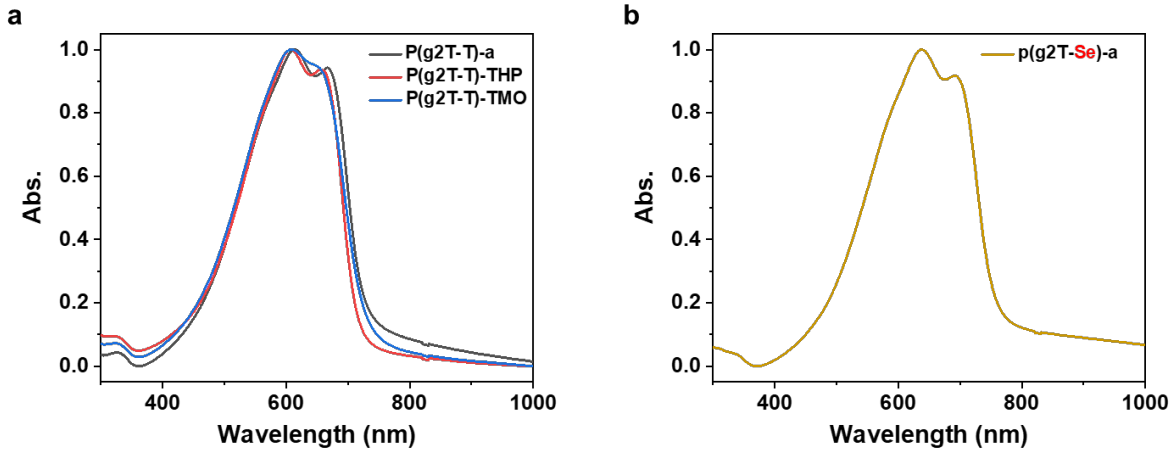

Supplementary Fig. 32 | UV-Vis absorption of p(g2T-T)-a, p(g2T-T)-THP, and p(g2T-T)-TMO (a), and p(g2T-Se)-a (b).

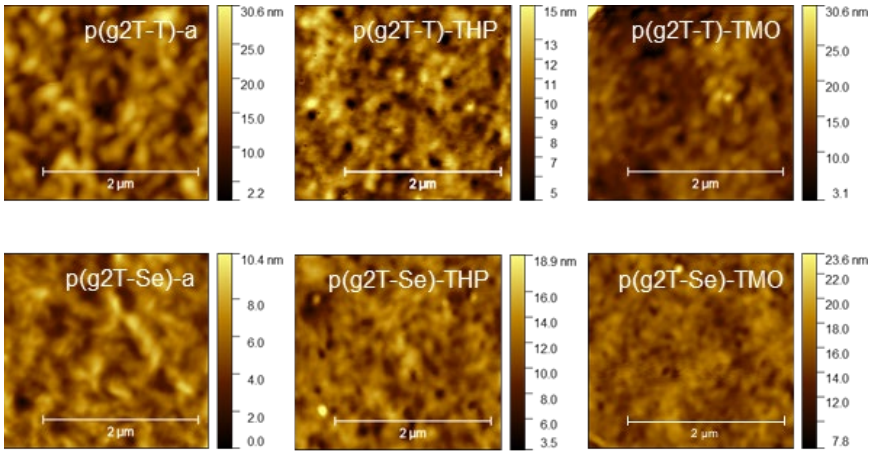

Supplementary Fig. 33 | AFM morphological characterization of the semiconducting polymers.

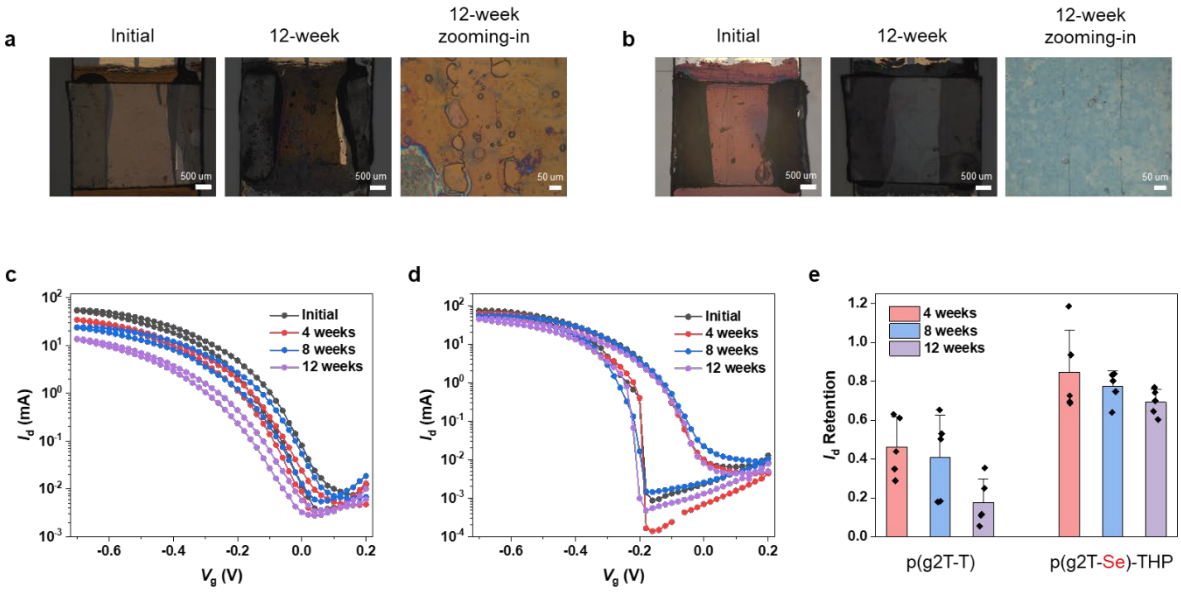

Supplementary Fig. 34 | Electrical stability test for the semiconducting polymers. a, **b**, Optical microscopy images showing the initial and explanted films of p(g2T-T) (**a**) and p(g2T-Se)-THP (**b**) after 12-week implantation. **c**, **d**, OECT transfer scans for p(g2T-T) (**c**) and p(g2T-Se)-THP (**d**) films measured at different implantation time points. **e**, Retention ratio of on-currents (I_d) for both films. Values represent mean values ± s.d. (n = 5 biologically independent samples).

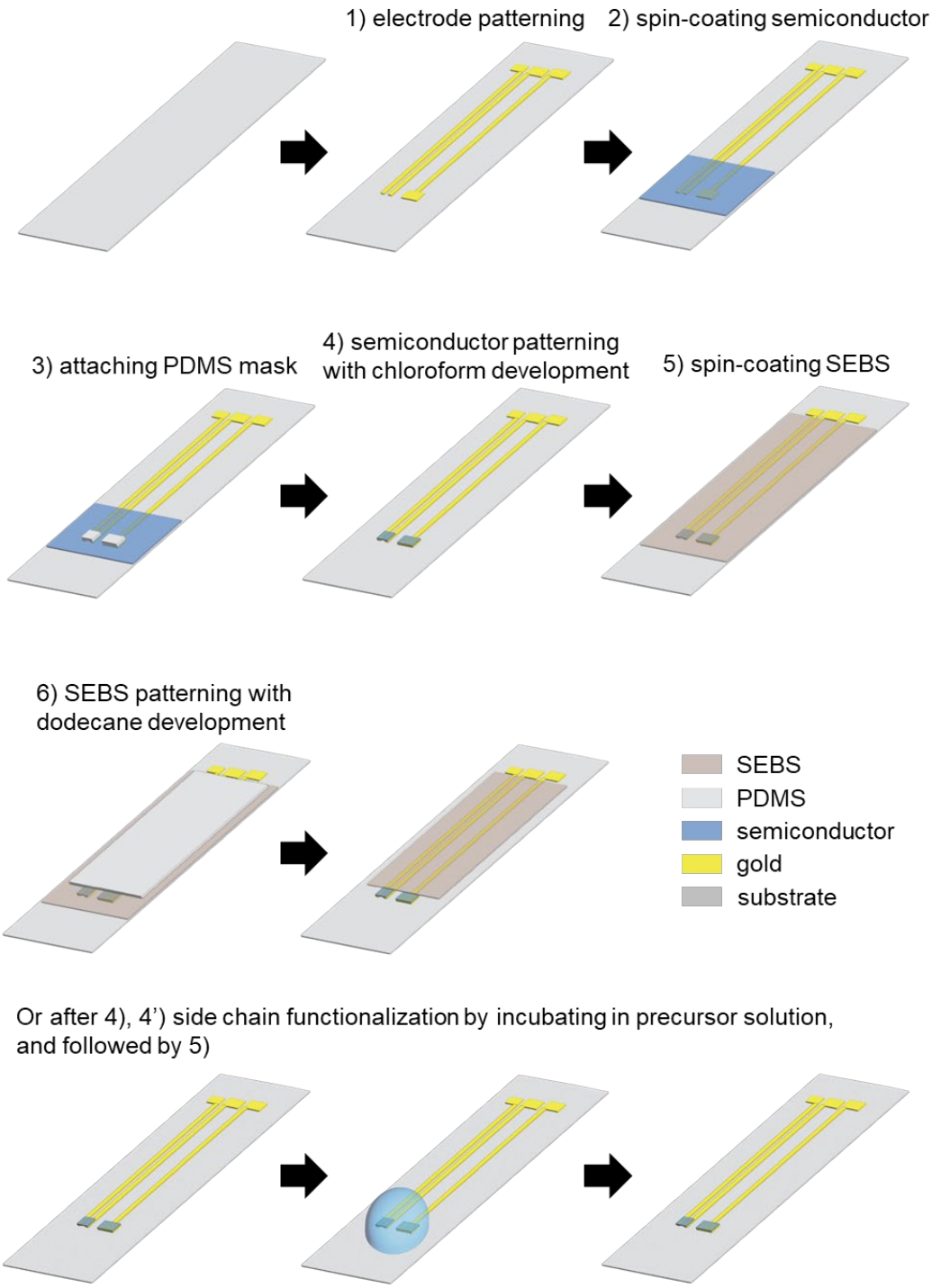

Supplementary Fig. 35 | Fabrication process for the implantable OECT devices.

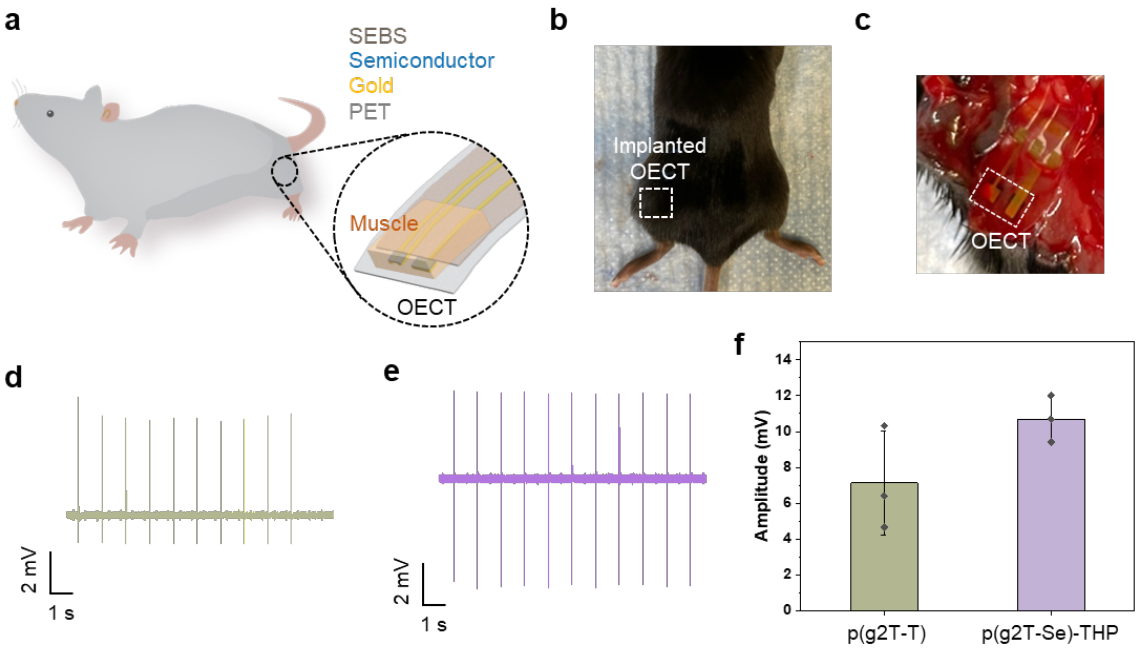

Supplementary Fig. 36 | EMG recording with the implantable OECT devices. a, Schematic illustrating the subcutaneous implantation of an OECT sensor in a live mouse, for recording EMG signals from gastrocnemius medialis (GM) muscle. **b**, Photograph showing the location of the implanted OECT under the skin. **c**, Photograph showing the OECT on the muscle. **d**, **e**, Representative EMG signals recorded by a p(g2T-T)-based OECT (**d**) and a p(g2T-Se)-THP-based OECT (**e**) after 17 days of implantation. **f**, Comparison of EMG signal amplitudes recorded by the two polymer semiconductors. Three individual OECT sensors were implanted and measured for each polymer. Values represent mean values ± s.d (n = 3 biologically independent samples).

Supplementary Tables

Supplementary Table 1 | Comparison of immune-compatible semiconducting polymers with conventional methods for suppressing FBR

Strategies	Immune-compatible semiconducting polymers	Immune-compatible surface coating	Anti-inflammatory drug-releasing
Tissue-interface schematics	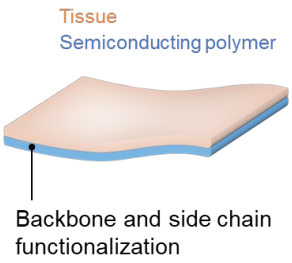	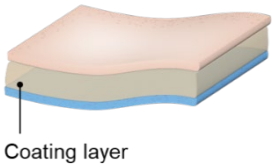	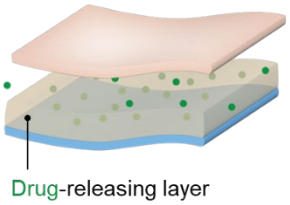
Sensing-tissue distance	Direct interface	Increased	Increased
Interfacial impedance	Low	High	High
Sensing amplitude	High	Low	Low
Efficacy lifetime	Long	Long	Limited
Adverse effect	Not known	Not known	Drug diffusion potentially to surrounding tissues

Supplementary Table 2 | Molecular weights of polymers

Polymers	M_n (kDa)	M_w (kDa)	PDI
P(g2T-T)-a	30	62	2.1
P(g2T-Se)-a	52	130	2.5

Supplementary Table 3 | PCR primer sequence of murine collagen I, murine collagen III, and β-actin.

Murine collagen I forward	5′-GAG CGG AGA GTA CTG GAT CG-3′
Murine collagen I reverse	5′-GTT CGG GCT GAT GTA CCA GT-3′
Murine collagen III forward	5′-AGC TTT GTG CAA AGT GGA ACC TGG-3′
Murine collagen III reverse	5′-CAA GGT GGC TGC ATC CCA ATT CAT-3′
Murine β-Actin forward	5′-GCC TCC CTT CTT GGG TAT GGA A-3′
Murine β-Actin reverse	5′-CAG CTC AGT AAC AGT CCG CC-3′

Supplementary Table 4 | Comparison of our immune-compatible semiconductor polymer (as represented by p(g2T-Se)-THP) to previously reported semiconducting polymers, conducting polymers, and composite.

Materials[i]		Electrical performance	Multifunctionality	Softness	Biocompatibility[ii] (testing method)	Refs
Semiconductors	p(g2T-Se)-THP	Mobility> 1 $cm^2 V^{-1} s^{-1}$	Semiconductor	~250 MPa[iii]	68% decrease in collagen density (MT, HE, IF, biomarkers, PCR, blood and organ toxicities)	This work
	Bioadhesive semiconductors	Mobility~ 1 $cm^2 V^{-1} s^{-1}$	Semiconductor	0.95 MPa	Less fibrosis than SEBS post 4-week (MT, IF)	2
	PDPPEDOT /Pluronic 127 NPs/PNIPAM	N/A	Photothermal	N/A	Low cytotoxicity with HeLa cells	3
	Quantum dots $CuInSe_2$@ZnS:Al/PMMA	PLQY~43.6%	Light absorption/emission	N/A	Low cytotoxicity and fibrosis (MT, HE)	4
Conductors	Whiskered Au nanosheets/TPU	Conductivity~ 1600 S cm^{-1}	Conductor	>61.3 MPa	Low cytotoxicity with L929 cells	5
	Ag/Au nanowires/SBS/ hexylamine	Conductivity~ 41,850 S cm^{-1}	Conductor	3.28 MPa	~30% fibrotic area post 3-week (MT, HE)	6
	CNT/polyrotaxane	Admittance~ 100 mS cm^{-2}	Conductor	10 kPa	Moderate irritant and fibrosis (HE)	7
	rGO/PVA/PAA-NHS	Conductivity~2.6 S m^{-1}	Conductor	293 kPa	Similar to gold (HE, IF)	8
	Porous liquid metal/ε-PL/PU	Conductivity ~2.0×10^5 S/m	Conductor	1.5 MPa	Antimicrobial and low cytotoxicity	9

[i]PNIPAM denotes poly(*N*-isopropylacrylamide); PMMA denotes poly(methyl methacrylate); TPU denotes medical-grade thermoplastic polyurethane; SBS denotes poly(styrene-butadiene-styrene); rGO denotes reduced graphene oxide; PVA denotes poly(vinyl alcohol); PAA-NHS denotes poly(acrylic acid) grafted with *N*-hydroxysuccinimide ester; ε-PL denotes epsilon polylysine.

[ii]Biocompatibility evaluation methods in vivo: MT, Masson's trichrome staining; HE, hematoxylin and eosin staining; IF, immunofluorescence staining.

[iii]Value estimated from ref[6].

Supplementary References

1 Li, N. *et al.* A universal and facile approach for building multifunctional conjugated polymers for human-integrated electronics. *Matter* **4**, 3015-3029, (2021).

2 Li, N. *et al.* Bioadhesive polymer semiconductors and transistors for intimate biointerfaces. *Science* **381**, 686-693, (2023).

3 Wu, Y., Wang, K., Huang, S., Yang, C. & Wang, M. Near-Infrared Light-Responsive Semiconductor Polymer Composite Hydrogels: Spatial/Temporal-Controlled Release via a Photothermal "Sponge" Effect. *ACS Appl Mater Interfaces* **9**, 13602-13610, (2017).

4 McHugh, K. J. *et al.* Biocompatible near-infrared quantum dots delivered to the skin by microneedle patches record vaccination. *Science Translational Medicine* **11**, eaay7162, (2019).

5 Lim, C. *et al.* Facile and Scalable Synthesis of Whiskered Gold Nanosheets for Stretchable, Conductive, and Biocompatible Nanocomposites. *ACS Nano* **16**, 10431-10442, (2022).

6 Choi, S. *et al.* Highly conductive, stretchable and biocompatible Ag-Au core-sheath nanowire composite for wearable and implantable bioelectronics. *Nat Nanotechnol* **13**, 1048-1056, (2018).

7 Sekitani, T. *et al.* Ultraflexible organic amplifier with biocompatible gel electrodes. *Nat Commun* **7**, 11425, (2016).

8 Deng, J. *et al.* Electrical bioadhesive interface for bioelectronics. *Nat Mater* **20**, 229-236, (2021).

9 Xu, Y. *et al.* Porous liquid metal–elastomer composites with high leakage resistance and antimicrobial property for skin-interfaced bioelectronics. *Science Advances* **9**, eadf0575, (2023).